

Magnetophotogalvanic Effects Driven by Terahertz Radiation in CdHgTe Crystals with Kane Fermions

M. D. Moldavskaya¹, L. E. Golub¹, V. V. Bel'kov², S. N. Danilov¹, D. A. Kozlov¹, J. Wunderlich¹, D. Weiss¹, N. N. Mikhailov³, S. A. Dvoretzky³, S. S. Krishtopenko⁴, B. Benhamou-Bui⁴, F. Teppe⁴, and S. D. Ganichev¹

¹*Physics Department, University of Regensburg, 93040 Regensburg, Germany*

²*Ioffe Institute, 194021 St. Petersburg, Russia*

³*Rzhanov Institute of Semiconductor Physics, 630090 Novosibirsk, Russia and*

⁴*Laboratoire Charles Coulomb (L2C), UMR 5221 CNRS-Université de Montpellier, F-34095 Montpellier, France*

We report on the observation and comprehensive study of the terahertz radiation induced magneto-photogalvanic effect (MPGE) in bulk CdHgTe crystals hosting Kane fermions. The MPGE has been detected in Cd_xHg_{1-x}Te films with Cd contents $x = 0.15$ and 0.22 subjected to an in-plane magnetic field. At liquid helium temperature we observed multiple resonances in MPGE current upon variation of magnetic field. In the $x = 0.22$ with noninverted band structure, the resonances are caused by cyclotron resonance (CR) and photoionization of an impurity level. In the $x = 0.15$ films with an inverted band structure, they originate from the CR and interband optical transitions. Band structure calculated by the Kane model perfectly describes positions of all resonances. In particular, the resonant MPGE caused by interband transitions excited by THz radiation is caused by the gapless energy spectrum of Kane fermions realized in materials with certain Cd contents and temperature range. In addition to the resonant MPGE current we detected a nonresonant one due to indirect optical transitions (Drude-like). This contribution has a nonmonotonic magnetic field dependence increasing linearly at low magnetic field B , approaching a maximum at moderate field and decreasing at high B . While the nonresonant MPGE decreases drastically with increasing temperature, it is well measurable up to room temperature. The developed theory demonstrates that the MPGE current arises due to cubic in momentum spin-dependent terms in the scattering probability. The asymmetry caused by these effects results in a pure spin current which is converted into an electric current due to the Zeeman effect.

I. INTRODUCTION

Three-dimensional topological semimetals are characterized by bulk band crossings in their electronic structures, resulting in gapless electronic excitations and distinctive topological properties that contribute to unusual physical phenomena. The last decade has seen a surge in research activity in this field, driven by accurate theoretical predictions, precise material synthesis, and advanced characterization techniques. Dirac and Weyl materials are notable examples, with pseudo-relativistic band dispersion near the Fermi level, where low-energy fermionic excitations, namely Dirac and Weyl fermions, resemble elementary particles from quantum field theory. Nevertheless, massless 3D Kane fermions, a unique pseudo-relativistic quasiparticle, have been identified in bulk Cd_xHg_{1-x}Te near the semiconductor-to-semimetal topological phase transition at a critical cadmium concentration of $x_C \approx 0.17$ for a temperature of 2 K, and described by a simplified Kane model [1]. These massless 3D particles feature an energy dispersion with the cones intersected by an additional flat band at the vertex, unlike any known relativistic particle. Unlike Dirac fermions, Kane fermions are not protected by symmetry or topology, but they respect time-reversal symmetry and can be created through appropriate band engineering.

Teppe et al. [2] analyzed the physical properties of these particles, and showed that their rest mass can be inverted near the topological phase transition, while their velocity remains constant, demonstrating their universal

relativistic behavior. In bulk CdHgTe alloys, the narrow band-gap (the rest mass of Kane electrons) can indeed be tuned from positive to negative by varying temperature [3], chemical composition [4], hydrostatic pressure [5], or short-range disorder [6]. Moreover, when the band ordering is inverted, 3D massive Kane electrons are accompanied by 2D topological Volkov-Pankratov states at the interfaces [7, 8] which have also been observed and characterized in Refs. [9–12]. Kane fermions are not exclusive to Hg-based materials; they also exist in cadmium arsenide (Cd₃As₂), coexisting with three-dimensional Dirac fermions when the Fermi level is high in the conduction band [13]. However, their physical properties and theoretical models are still being explored, particularly in CdHgTe compounds. For example, recent theoretical work on the relativistic collapse of their Landau levels under different orientations of crossed electric and magnetic fields suggests that Kane fermions are “complex” particle consisting of two nested Dirac particles with different rest masses [14].

Experimentally Kane fermions have been studied using a variety of optical and opto-electronic techniques including magneto-spectroscopy through absorption, reflection, or emission experiments, as well as, photoconductivity and photogalvanic effects, see, e.g., Refs. [1, 2, 5, 12, 15–20]. Moreover, Kane fermion mobility have been shown to be as high as 10^6 cm²/V·s near the topological phase transition [21], resulting in strong nonlinear THz dynamics recently observed in CdHgTe [22]. Furthermore, a giant non-saturating magnetoresistance has been observed

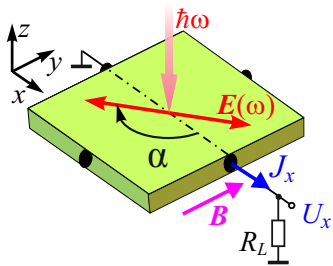


FIG. 1. Experimental setup. The sample is excited by normally incident linearly polarized terahertz radiation. In-plane orientation of the radiation electric field \mathbf{E} is defined by the azimuth angle α counted from x -axis. The magnetic field \mathbf{B} is applied in the plane along the y -axis. The photosignal is measured from the pair of contacts made along the x -direction as a voltage drop U_x across the load resistance $R_L = 50 \Omega$.

in gapless CdHgTe due to the gap opening in Landau-quantized Kane electrons [23]. Finally, the specific origin of the Kane electrons suppresses non-radiative Auger recombination between their non-equidistant Landau levels, suggesting potential for THz Landau lasers [24].

In this study, we present the first observation and analysis of magneto-photogalvanic effects (MPGE) in bulk CdHgTe crystals with different cadmium contents. MPGE is an effect where an ac electric field is converted into dc electric current which requires an external magnetic field, for reviews see, e.g., Refs. [25–27]. Our experimental and theoretical work explores MPGE driven by Drude absorption of THz radiation by Kane fermions and resonant MPGE resulting from inter-Landau level transitions, interband optical transitions, and ionization of impurity levels. The multiple resonances of the MPGE current in the magnetic field have been uniquely identified with the corresponding optical transitions considering the band structure calculated in the frame of $\mathbf{k} \cdot \mathbf{p}$ theory. The developed theory and experiments show that the MPGE is excited in the bulk of the material and is caused by spin current excitation, which is converted into an electrical current by the Zeeman effect. We show that the pure spin current is caused by the asymmetric scattering of the photoexcited carriers taking into account terms cubic in momentum in the scattering probability.

II. EXPERIMENTAL METHODS AND SAMPLES

MPGE was studied in molecular beam epitaxy grown $\text{Cd}_x\text{Hg}_{1-x}\text{Te}$ films having a common general layer structure and Cd content $x = 0.15$ (sample A) and 0.22 (sample B). The films were grown on (013)-oriented GaAs substrates followed by a 30 nm ZnTe buffer layer and a 6 μm layer of CdTe. The film thickness with constant Cd content was 4 μm (sample A) and 7 μm (sample B). More details on the sample's composition and parameters can be found in Ref. [12] where the same samples were stud-

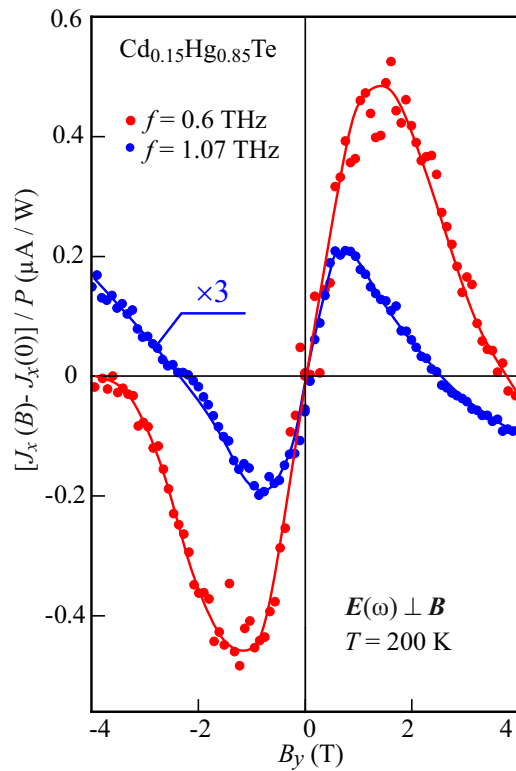


FIG. 2. Magnetic field dependence of the photocurrent $J_x(B_y)$ measured in the sample A ($x = 0.15$) at $T = 200$ K. The photocurrent is measured for the radiation electric field perpendicular to the magnetic field direction ($\alpha = 0$) and two frequencies $f = 0.6$ and 1.07 THz. A small zero magnetic field response $J_x(0)$ is subtracted from the current $J_x(B_y)$ and the data are normalized to the radiation power P . Normalized photocurrent at zero magnetic field, $J_x(0)/P$, and radiation power P in these measurements were (i) $-0.1 \mu\text{A}/\text{W}$ and 360 W (red curve, $f = 0.6$ THz); (ii) $-0.014 \mu\text{A}/\text{W}$ and 4200 W (blue curve, $f = 1.07$ THz), respectively. Note that the data for $f = 1.07$ THz are multiplied by factor 3. The main panel shows the photocurrent J_x detected in the direction perpendicular to the magnetic field B_y .

ied. The square shaped samples with the sides oriented along $[110]$ and $[\bar{1}\bar{1}0]$ have a sample size of $5 \times 5 \text{ mm}^2$. Ohmic indium contacts were soldered to the center of the sample edges, see Fig. 1. The transport and magneto-transport characteristics of the samples are presented in the Appendix A. The samples were placed in a temperature variable optical cryostat with z -cut crystal quartz windows and split coil magnet allowing measurements in the Voigt geometry. In the experiments we used temperatures from 4.2 to 300 K and the magnetic field up to 4 T.

The photocurrent was studied using a line-tunable optically pumped pulsed molecular laser with NH_3 and CH_3F gases as active media [28–30]. The laser operated at $f = 0.6$ THz ($\lambda = 496 \mu\text{m}$, $\hbar\omega = 2.5$ meV), $f = 1.07$ THz ($\lambda = 280 \mu\text{m}$, $\hbar\omega = 4.4$ meV), $f = 2.02$ THz ($\lambda = 148 \mu\text{m}$, $\hbar\omega = 8.4$ meV), and 3.33 THz

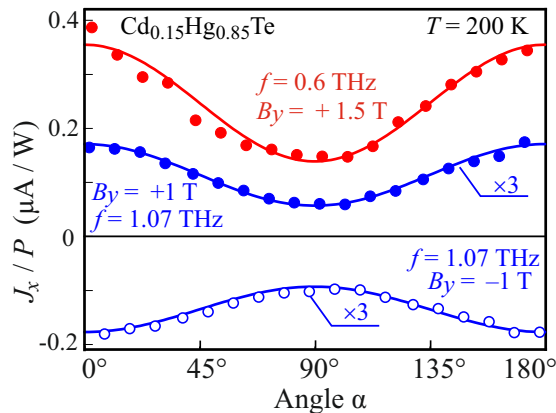


FIG. 3. Normalized photocurrent J_x/P as a function of the azimuth angle α measured in sample A ($x = 0.15$) subjected to magnetic field B_y and excited by radiation at $f = 0.6$ and 1.07 THz. The data are obtained at $T = 200$ K. The radiation power P in these measurements was 360 and 4200 W for the frequencies $f = 0.6$ and 1.07 THz, respectively. The lines are fits according to Eq. (32).

($\lambda = 90.5 \mu\text{m}$, $\hbar\omega = 13.7$ meV). The pump laser was a line-tunable transversely-excited atmospheric pressure (TEA) CO_2 . The molecular laser generated single pulses with a duration of about 100 ns and a repetition rate of 1 Hz. The laser radiation power was approximately 100 kW. The peak power of the radiation was monitored by infrared and terahertz photon-drag detectors [31, 32]. The beam positions and profiles were controlled by a pyroelectric camera. The nearly Gaussian beam was focused on the sample using an off-axis parabolic mirror resulting in a spot size of 1.5 to 3 mm, depending on the radiation frequency. As we show below, the MPGE effect increases drastically (by four orders of magnitude) with decreasing temperature and saturates with the radiation intensity I at high I . Therefore, to avoid the photocurrent nonlinearity we strongly reduced I for low- T measurements.

The experiments were performed using normal incident linearly polarized radiation, see Fig. 1. In order to vary the angle between the polarization vector of the linearly polarized light and the magnetic field, we used crystalline quartz $\lambda/2$ -plates. Rotation of the half-wave plate allowed us to vary the azimuth angle α from 0° to 180° , covering all possible orientations of the electric field vector in the (xy) plane with respect to the in-plane magnetic field. In the following we choose $y \parallel \mathbf{B}$ and the angle $\alpha = 0$ is zero along the x -direction, perpendicular to vector \mathbf{B} , see Fig. 1. The terahertz radiation induces free carrier absorption in the lowest conduction subband $e1$ because the photon energies are smaller than the energy gap. For certain magnetic field strengths, however, the radiation also excites inter-Landau level transitions, causing the resonant MPGE current. The photocurrent J_x was measured in unbiased structures from the voltage drop U across a load resistor $R_L = 50 \Omega$ in closed circuit

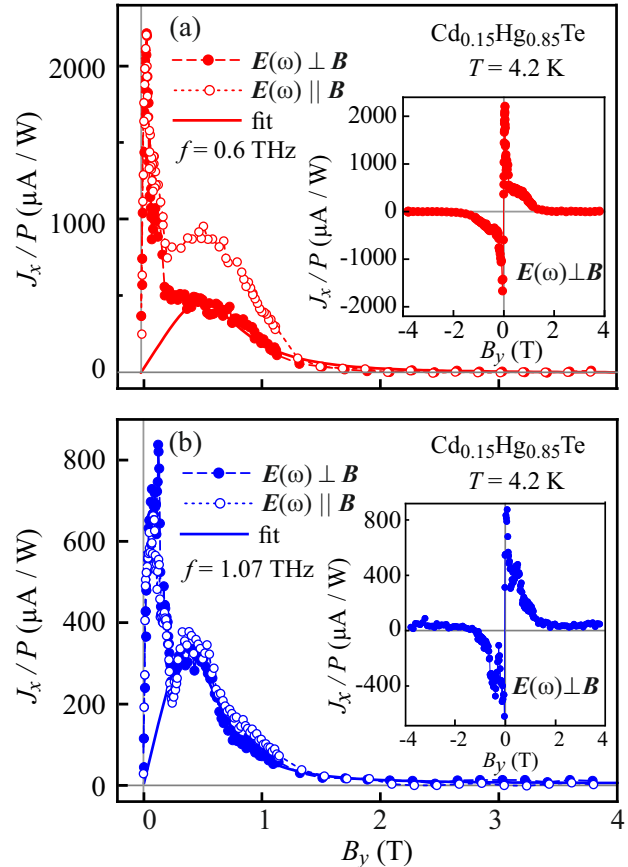


FIG. 4. Magnetic field dependencies of the photocurrent J_x normalized to the power P obtained at $T = 4.2$ K and for the radiation electric field perpendicular and parallel to the magnetic field B_y . Data are shown for the radiation frequencies $f = 0.6$, panel (a), and 1.07 THz, panel (b). The insets show $J_x(B_y)$ for both magnetic field polarities and $\mathbf{E}(\omega) \perp \mathbf{B}$. The radiation power P in these measurements were 0.06 W for both frequencies. The solid curves are fits according to Eq. (33).

configuration. The voltage was recorded with a storage oscilloscope and the photocurrent was calculated according to $J_x = U/R_{\parallel}$, where $R_{\parallel} = R_s \times R_L / (R_s + R_L)$ and R_s is the sample resistance. The measured photocurrent pulses of 100 ns duration reflected the corresponding laser pulses.

III. EXPERIMENT

A. Results for $\text{Cd}_x\text{Hg}_{1-x}\text{Te}$ films with $x = 0.15$

We begin with the data obtained on sample A with $x = 0.15$. Figure 2 shows the magnetic field dependence of the photocurrent excited in the direction perpendicular to the in-plane magnetic field B_y by linearly polarized radiation with $\mathbf{E}(\omega) \perp \mathbf{B}$. The data are obtained at $T = 200$ K. To emphasize the magnetic field induced

photoresponse in this plot we have subtracted the photocurrent generated at $B = 0$. The photocurrent is odd in a magnetic field and depends non-monotonically on B : at low magnetic fields it increases almost linearly, approaches a maximum, and then decreases and changes its sign (see the data for $f = 1.07$ THz). Such a qualitative behavior is observed for all frequencies studied. We observed that increasing the frequency reduces the photocurrent magnitude at the maximum, and shifts the maximum as well as the inversion point to lower magnetic fields. At low power, the photocurrent depends linearly on the radiation power, and saturates as the power increases. To study the photoresponse in the linear regime, in all measurements below we first measured the power dependences and then substantially reduced the radiation power until reaching the regime $J \propto P \propto E^2(\omega)$ [33].

The observed magnetic field induced photocurrent consists of a polarization independent part and a part varying with the azimuth angle α as $\cos(2\alpha)$. Figure 3 shows, as an example, several characteristic traces obtained at two frequencies and for the magnetic field strength corresponding to the signal maximum. The data obtained at $B_y = \pm 1$ T and $f = 1.07$ THz demonstrate that both, polarization dependent and independent photocurrents, are odd in B_y .

Cooling to 4.2 K results in a drastic increase of the photocurrent amplitude by more than three orders of magnitude, compare Figs. 4 and 2. Moreover, the nonmonotonic photocurrent detected at high temperature is now accompanied by resonances that appear at low magnetic fields and have about twice the magnitude of the nonresonant one. The insets in Fig. 4 show that both types of the photocurrent reverse sign when the magnetic field polarity is changed.

Comparing Figs. 2 and 4, we see that lowering temperature causes the maximum of the nonresonant photocurrent narrow and to shift to lower magnetic fields. Furthermore, at high field, the nonresonant current disappears and the sign reversal with increasing magnetic field strength observed at high temperatures, is absent.

Figure 5 shows a zoom of the low magnetic field range where the photocurrent resonances are detected. Experiments are performed for two different orientations of the radiation electric field with respect to the magnetic field ($\mathbf{E} \parallel \mathbf{B}$ and $\mathbf{E} \perp \mathbf{B}$). The data reveal two types of resonances on top of the nonresonant photoresponse: (i) independent of the radiation polarization (we will label them R), and (ii) excited only for $\mathbf{E} \perp \mathbf{B}$ (labeled as CR). As we show in Sec. V, CR-type resonances arise from transitions between the electron Landau levels (cyclotron resonances), while R-type resonances are caused by interband transitions between levels of heavy holes and electrons in an inverted band structure. Figure 6 shows the photocurrents measured with higher resolution in the low magnetic field region. The data are shown for four frequencies at CR-active polarization. It can be seen that with increasing frequency, more R-type resonances appear on the $J_x(B_y)$ dependence. CR-type resonances

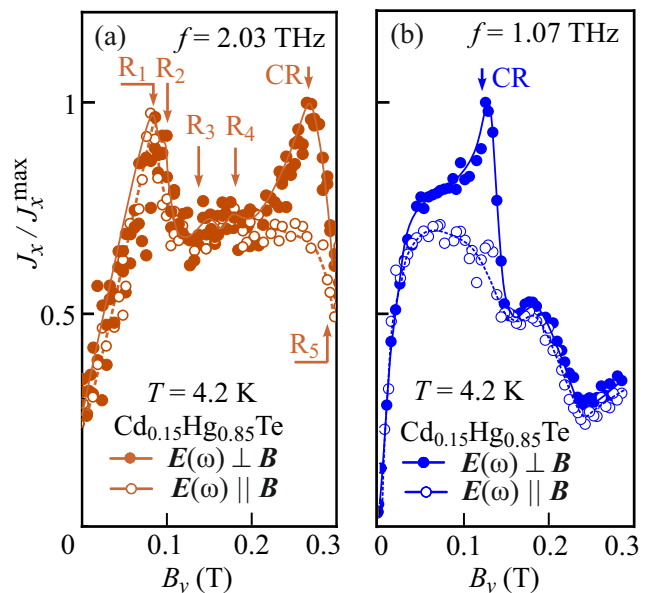


FIG. 5. Low-field zoom of the magnetic field dependencies of the photocurrent J_x normalized to the power P obtained in sample A at $T = 4.2$ K. The data are presented for the radiation electric fields perpendicular and parallel to the magnetic field \mathbf{B} for the radiation frequencies $f = 2.03$, panel (a), and 1.07 THz, panel (b). Downward arrows indicate the positions of the CR- and R-type resonances, for the corresponding magnetic fields see Table 1. The low magnetic field data with higher resolution (smaller magnetic field step is used) are shown in Fig. 6 and the corresponding optical transitions are sketched in the calculated Landau level diagrams and discussed in the Sec. V. The radiation power P in these measurements were 0.1 and 10 W for the frequencies $f = 1.07$ and 2.03 THz, respectively.

are clearly seen at 1.07 and 2.03 THz. At a frequency of 3.33 THz, the CR-type resonance is visible as a difference between the active and inactive polarization, see the inset in Fig. 6(b).

B. Results for $\text{Cd}_x\text{Hg}_{1-x}\text{Te}$ films with $x = 0.22$

Now we turn to the results obtained for sample B with $x = 0.22$. Figure 7 shows the magnetic field dependence of the photocurrent detected at 250 K. As for sample A ($x = 0.15$), the signal has a nonmonotonic magnetic field dependence at high temperatures and changes its sign at high magnetic fields. Reducing the temperature down to $T = 4.2$ K strongly increases the magnitude of the nonresonant photocurrent maximum, and, for $\mathbf{E} \perp \mathbf{B}$ a nonresonant photocurrent is superimposed on the resonant one, see Fig. 8. Note that at low temperatures the currents detected in sample B have the opposite sign to those observed at $T = 250$ K and to the photocurrents generated in sample A. The signal shows a characteristic polarization dependence of the photocurrent. The signal is odd in the magnetic field, and its polarization depen-

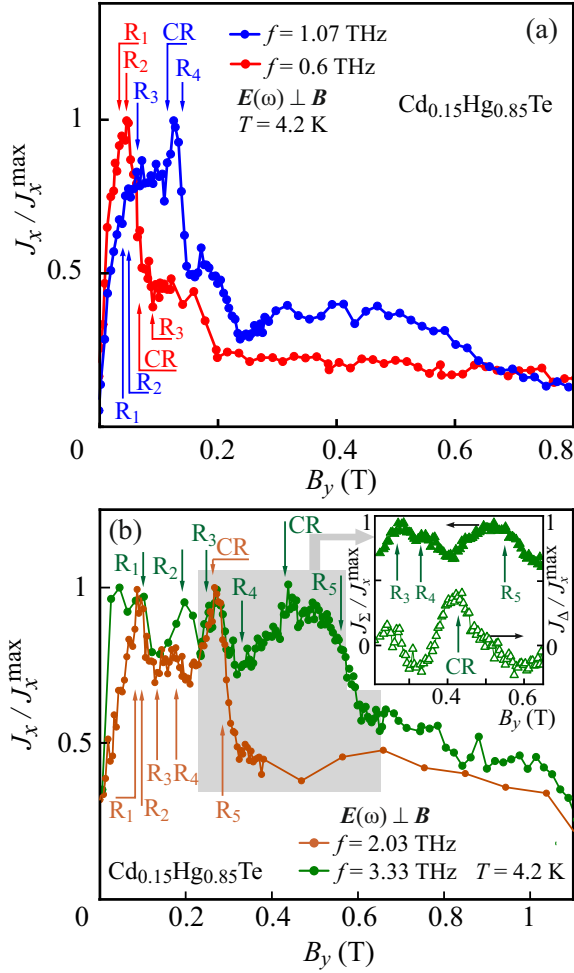


FIG. 6. Magnetic field dependencies of the photocurrents at frequencies $f = 1.07$ and 0.6 THz (a), and $f = 2.03$ and 3.33 THz (b) measured at $T = 4.2$ K with polarization $\mathbf{E}(\omega) \perp \mathbf{B}$. The photocurrent J_x is normalized by the maximum photocurrent value J_x^{\max} . Downward arrows indicate the positions of the CR- and R-type resonances, for the corresponding magnetic fields see Table I. Corresponding optical transitions are sketched in the calculated Landau level diagrams and discussed in the Sec. V. The inset shows the polarization independent and the polarization dependent photocurrents calculated according to $J_\Sigma = [J(\alpha = 0) + J(\alpha = 90^\circ)]/2$ and $J_\Delta = [J(\alpha = 0) - J(\alpha = 90^\circ)]/2$. The data are obtained at a higher resolution (smaller magnetic field step is used), and shown for the magnetic field range highlighted by the gray area where CR is expected. The plot is used to resolve the CR resonance, which vanish for $\mathbf{E}(\omega) \parallel \mathbf{B}$ ($\alpha = 90^\circ$), hidden by the neighboring polarization independent R_4 - and R_5 -resonances.

dence is well described by the function $J \propto \cos(2\alpha)$, see Figs. 8 and 9.

As mentioned above, in addition to the non-resonant photocurrent, we also detected a resonant contribution in sample B at $T = 4.2$ K. The resonant peak is observed at CR-active polarization $\mathbf{E}(\omega) \perp \mathbf{B}$ and is absent at pas-

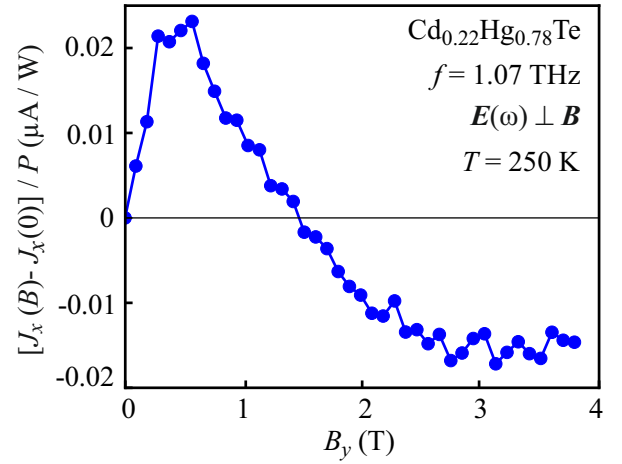


FIG. 7. Magnetic field dependence of the normalized photocurrent $[J_x(B_y) - J_x(0)]/P$ measured for sample B ($x = 0.22$), $\mathbf{E}(\omega) \perp \mathbf{B}$, frequency $f = 0.6$ THz, and power $P = 0.6$ W.

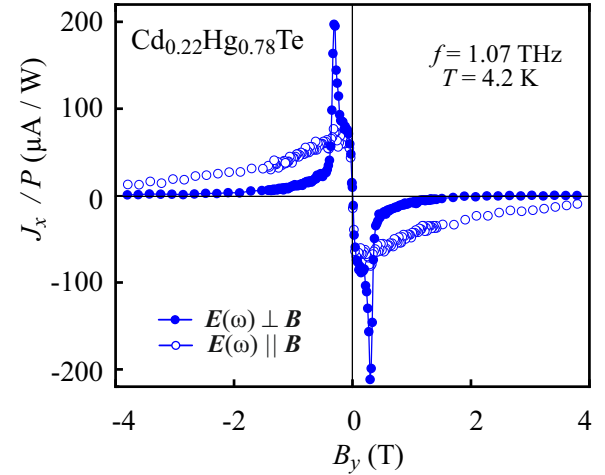


FIG. 8. Magnetic field dependence of the normalized photocurrents $J_x(B_y)/P$ measured in the sample B ($x = 0.22$) at $T = 4.2$ K. The data are presented for the radiation electric field $\mathbf{E}(\omega)$ perpendicular and parallel to the magnetic field \mathbf{B} for the radiation frequency $f = 1.07$ THz and power $P = 0.6$ W.

sive polarization $\mathbf{E}(\omega) \parallel \mathbf{B}$, see Fig. 8. The frequency dependence of the CR resonance positions for both samples is shown in the inset of Fig. 10 (a), demonstrating that the resonance magnetic fields increase with increasing frequency. Polarization-independent resonances denoted as \mathcal{R} are also observed in the sample B at high frequencies, see Fig. 10. However, unlike sample A where multiple R-type of resonances were detected, see Fig. 6, the resonances \mathcal{R} in sample B appear as only a single line for each frequency. Note that the maximum photocurrent value at the same frequency in the sample B is 4-5 times smaller than in the sample A.

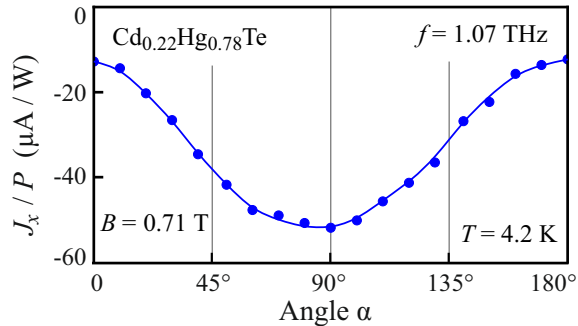


FIG. 9. Dependence of the normalized photocurrent J_x/P on the azimuth angle α measured in sample B ($x = 0.22$) subjected to a magnetic field $B_y = 0.71$ T and excited by radiation with $f = 1.07$ THz. The data were obtained for $T = 4.2$ K. The radiation power P in this measurement was 0.6 W. Lines are fits to Eq. (32).

IV. THEORY

The MPGE current can arise owing to two distinct microscopic grounds. The first mechanism is related to spin properties of carriers. With account for the spin-orbit interaction, the fluxes of particles in each spin subband, \mathbf{i}_\uparrow and \mathbf{i}_\downarrow , are generated under optical absorption, and the pure spin current

$$\mathcal{J} = \frac{\mathbf{i}_\uparrow - \mathbf{i}_\downarrow}{2} \quad (1)$$

is formed [31]. In bulk CdHgTe, the spin fluxes appear under radiation absorption due to the odd in momentum terms in the probability of the electron-phonon interaction. In the crystals of T_d symmetry the corresponding scattering matrix element has the following form

$$U_{\mathbf{k}'\mathbf{k}} = U_0 \left[1 + \xi \sum_{i=x',y',z'} \sigma_i K_i (K_{i+1}^2 - K_{i+2}^2) \right], \quad (2)$$

where $U_0(\mathbf{k}' - \mathbf{k})$ is the electron-phonon scattering matrix element without account for the non-centrosymmetry of the crystal, $x' \parallel [100]$, $y' \parallel [010]$, $z' \parallel [001]$ are the cubic axes, σ_i are the Pauli matrices, cyclic permutation of the indices is assumed, ξ is a material constant, and

$$\mathbf{K} = \mathbf{k} + \mathbf{k}'. \quad (3)$$

It follows from this expression that electrons with spins along and opposite to $\mathbf{B} \parallel y$ have different scattering matrix elements $U_{\mathbf{k}'\mathbf{k}}^\pm$ given by

$$U_{\mathbf{k}'\mathbf{k}}^\pm = U_0 \left(1 \pm \xi \sum_{i,j,l=x,y,z} a_{ijl} K_i K_j K_l \right), \quad (4)$$

where the coefficients a_{ijl} are determined by the orientation of the coordinate system (x, y, z) in respect to the cubic axes.

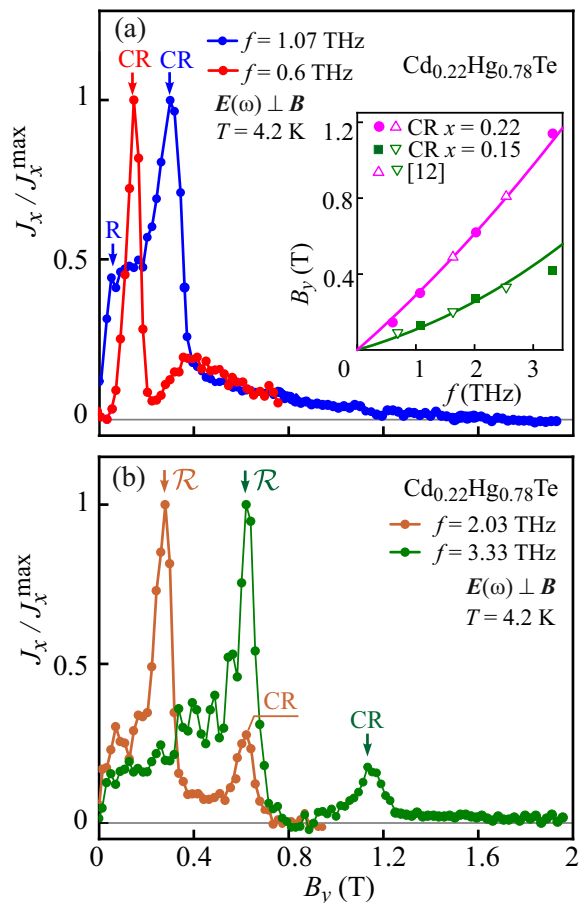


FIG. 10. Low-field part of the magnetic field dependencies of the photocurrents $J_x(B_y)$ obtained at $T = 4.2$ K and normalized to their maxima. The data are presented for sample B ($x = 0.22$), the radiation electric field perpendicular to the magnetic field \mathbf{B} , and for the radiation frequencies $f = 0.6$, 1.07, 2.03, and 3.33 THz. The radiation power P in these measurements was 0.065 W ($f = 0.6$ THz); 0.6 W ($f = 1.07$ THz); 0.02 W ($f = 2.02$ THz); and 0.06 W ($f = 3.3$ THz). Arrows labeled CR show resonances, that are absent for the radiation electric field parallel to the magnetic field B_y . Arrows labeled by \mathcal{R} show resonances, that are insensitive to the radiation polarization. The corresponding magnetic fields are given in Table II. The inset shows the frequency dependencies of the CR position. Here open triangles are the CR positions obtained in Ref. [12] in the radiation transmission experiments. Lines are calculated frequency dependencies of the CR positions.

We develop a theory of MPGE for the relevant to the experiment case of Drude-like intraband radiation absorption. It is important that this type of absorption is caused not only by the carrier-photon interaction, but also by scattering. The cubic in momentum terms of opposite sign in the electron-phonon scattering matrix elements (4) result in an enhanced probability of the optical transition with the final state at positive (negative) momenta in the spin-down (spin-up) subband. Consequently, occupation of the final states is different, Fig. 11.

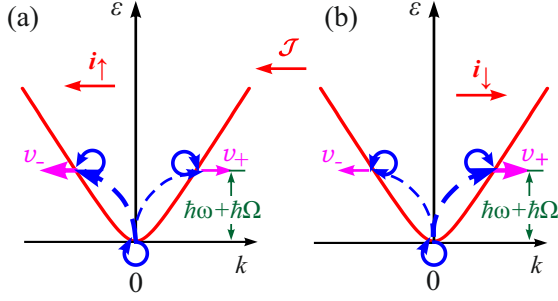


FIG. 11. Model of a pure spin photocurrent at zero magnetic field. Solid red curves show the Kane dispersion. Curved dotted and solid blue arrows sketch, respectively, scattering on phonons with the energy $\hbar\Omega$, and optical transition involving different virtual states in the same subband. Different thickness indicates difference in the probabilities of the corresponding processes. Horizontal magenta arrows show the resulting velocities for positive, v_+ , and negative, v_- , wavevectors k . Red horizontal arrows show spin fluxes generated in the spin-up, i_\uparrow , and spin-down, i_\downarrow , subbands as well as the total spin current \mathcal{J} .

This imbalance in each subband results in the oppositely directed spin fluxes i_\uparrow and i_\downarrow , and in the pure spin current \mathcal{J} , Eq. (1).

In the absence of magnetic field, the charge current

$$\mathbf{j} = e(i_\uparrow + i_\downarrow) \quad (5)$$

is not generated due to compensation of the fluxes of particles with opposite spins. The MPGE current is produced from the pure spin current by the Zeeman effect. Application of a magnetic field \mathbf{B} leads to the net carrier spin polarization S . For degenerate three-dimensional carriers we have

$$S = -\frac{1 - \sqrt{1 - g\mu_B B/\varepsilon_F}}{2(1 + \sqrt{1 - g\mu_B B/\varepsilon_F})}, \quad (6)$$

where ε_F is the Fermi energy and g is the electron Landé factor. Here we assumed $|g\mu_B B| < \varepsilon_F$, otherwise $S = -1/2$. At non-degenerate statistics, the average spin reads

$$S = -\frac{1}{2} \tanh\left(\frac{g\mu_B B}{2k_B T}\right). \quad (7)$$

Different numbers of the spin-up and spin-down carriers mean that the spin fluxes i_\uparrow , i_\downarrow have different absolute values. As a result, they do not compensate each other any more, and the charge current is generated under radiation absorption. The electric current density is given by a product of the pure spin current \mathcal{J} and the average spin S [31]:

$$\mathbf{j} = 4eS\mathcal{J}. \quad (8)$$

Competing is MPGE's orbital mechanism. In the magnetic field, there are spin-independent corrections to the

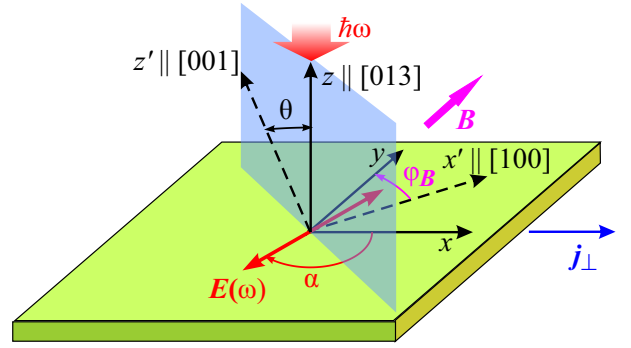


FIG. 12. Definition of the coordinate axes. In the Voigt geometry with radiation normally incident on the (013) sample surface, we introduce the axes (x, y) in the sample plane with $y \parallel \mathbf{B}$. The angle φ_B is an angle between \mathbf{B} and the axis $x' \parallel [100]$. The axes $z \parallel [013]$ and $z' \parallel [001]$ lie in the plane perpendicular to the axis x' (blue), and the angle between them $\theta = \arctan(1/3) \approx 18.4^\circ$. The angle α defines the polarization direction with $\alpha = 0$ corresponding to $\mathbf{E} \perp \mathbf{B}$.

scattering rates of the carriers, which are odd in \mathbf{B} and in the carriers' momentum. Such a diamagnetic contribution to the scattering matrix element in the crystals of T_d symmetry is given by

$$U_{\mathbf{k}'\mathbf{k}} = U_0 \left[1 + \zeta \sum_{i=x',y',z'} B_i K_i (K_{i+1}^2 - K_{i+2}^2) \right], \quad (9)$$

where \mathbf{K} is given by Eq. (3), and ζ is a material constant. Accordingly, the probability of radiation absorption is different for positive and negative carriers' momenta, and an asymmetric distribution of the carriers is formed in the momentum space as a result of optical absorption. This means an appearance of a net charge current in both spin subbands.

Both mechanisms of MPGE give comparable contributions to the charge current. In order to estimate the MPGE current we consider below the spin mechanism. We consider the limits of weak and strong magnetic fields and derive the frequency, magnetic field and radiation polarization dependencies of the MPGE current.

In the experiment, there are resonant and nonresonant contributions to the MPGE current. The nonresonant part is present at any polarization but it is polarization-dependent. The resonant contributions are of two types: one (R) exists at any polarization, and another (CR) is present only if the radiation electric field is not parallel to \mathbf{B} in the Voigt geometry. Below we develop a theory of MPGE for Kane fermions and consider the nonresonant part of the MPGE current caused by Drude-like intraband absorption in the conduction band. Then we investigate the CR and R peaks in the photocurrent caused by direct optical transitions between the conduction Landau subbands and interband transitions from the heavy-hole to the conduction band, respectively.

A. Classical magnetic fields

CdHgTe crystals have T_d point symmetry. This means that the MPGE current density, in the linear in the magnetic field regime, is described by two linearly independent constants, Φ_1 and Φ_2 [34]

$$\begin{aligned} j_{x'} &= \Phi_1 e_{x'} (B_{y'} e_{y'} - B_{z'} e_{z'}) I + \Phi_2 B_{x'} (e_{y'}^2 - e_{z'}^2) I, \\ j_{y'} &= \Phi_1 e_{y'} (B_{z'} e_{z'} - B_{x'} e_{x'}) I + \Phi_2 B_{y'} (e_{z'}^2 - e_{x'}^2) I, \\ j_{z'} &= \Phi_1 e_{z'} (B_{x'} e_{x'} - B_{y'} e_{y'}) I + \Phi_2 B_{z'} (e_{x'}^2 - e_{y'}^2) I. \end{aligned} \quad (10)$$

Here x', y', z' are the cubic axes, see Eq. (2), \mathbf{e} is the polarization vector, and I is the radiation intensity. This expression and the phenomenology for the Linear photogalvanic effect (LPGE) at $B = 0$ show that Φ_1 has a contribution from the Hall component of the LPGE current while Φ_2 describes the new contribution generated by the magnetic field.

Experiments are performed in the Voigt geometry with radiation normally incident on the (013) sample surface. Therefore we introduce the axes (x, y) in the sample plane with $y \parallel \mathbf{B}$. For the MPGE current perpendicular to \mathbf{B} we have from Eqs. (10)

$$\begin{aligned} j_x &= -\frac{B \cos 2\theta}{2} I \{ \Phi_2 \sin 2\varphi_B \\ &\quad + \Phi_1 [2e_x e_y \cos 2\varphi_B - (e_x^2 - e_y^2) \sin 2\varphi_B] \}, \end{aligned} \quad (11)$$

where φ_B is an angle between \mathbf{B} and the $x' \parallel [100]$ axis, and $\theta = \arctan(1/3) \approx 18.4^\circ$ is the angle between $z \parallel [013]$ and $z' \parallel [001]$, see Fig. 12.

It follows from Eqs. (6) and (7) that, in the linear in the magnetic field regime, the spin is given by

$$S = -\frac{g\mu_B B}{4\tilde{\varepsilon}}, \quad (12)$$

where $\tilde{\varepsilon}$ equals to $2\varepsilon_F$ and $k_B T$ at degenerate and non-degenerate statistics, respectively. Therefore in low fields, when the electric current is linear in B , the pure spin current \mathcal{J} is to be calculated at $B = 0$, see Eq. (8). The zero-field fluxes of particles in the spin subbands are given by [35]

$$\mathbf{i}_s = \sum_{\mathbf{k}, \mathbf{k}'} W_{\mathbf{k}'\mathbf{k}}^{(s)} [\mathbf{v}_{\mathbf{k}'} \tau(\varepsilon_{\mathbf{k}'}) - \mathbf{v}_{\mathbf{k}} \tau(\varepsilon_{\mathbf{k}})], \quad (13)$$

where summation is performed over wavenectors of electrons in the s 'th spin subband, $\varepsilon_{\mathbf{k}}$ is the Kane dispersion in the conduction band, Fig. 14

$$\varepsilon_{\mathbf{k}} = \varepsilon_g/2 + \sqrt{(\varepsilon_g/2)^2 + (\hbar v_0 k)^2} \quad (14)$$

with ε_g and v_0 being the energy gap and Kane velocity, the electron velocity $\mathbf{v}_{\mathbf{k}} = \hbar v_0^2 \mathbf{k} / (\varepsilon_{\mathbf{k}} - \varepsilon_g/2)$, and τ is the energy dependent momentum relaxation time. The

probability of the phonon-scattering assisted intra-band optical transition reads [35]

$$\begin{aligned} W_{\mathbf{k}'\mathbf{k}}^{(s)} &= \frac{2\pi}{\hbar} \sum_{\nu=\pm} [f_{\mathbf{k}}(1-f_{\mathbf{k}'})N_{\nu} - f_{\mathbf{k}'}(1-f_{\mathbf{k}})N_{-\nu}] \\ &\times \left| \frac{eU_{\mathbf{k}'\mathbf{k}}^s}{\hbar\omega^2} \mathbf{E} \cdot (\mathbf{v}_{\mathbf{k}} - \mathbf{v}_{\mathbf{k}'}) \right|^2 \delta(\varepsilon_{\mathbf{k}} + \hbar\omega - \nu\hbar\Omega - \varepsilon_{\mathbf{k}'}), \end{aligned} \quad (15)$$

where $U_{\mathbf{k}'\mathbf{k}}^s$ is the scattering matrix element Eq. (4), $N_{\nu} = N + (1 + \nu)/2$, N and Ω are the occupation number and frequency of phonons with the wavevector $\mathbf{q} = \mathbf{k}' - \mathbf{k}$, $f_{\mathbf{k}}$ is the Fermi-Dirac distribution function, and ω is the radiation frequency.

Treating the ξ -linear odd in momentum terms in the scattering matrix element (4) as small perturbations, we calculate the spin fluxes (13) and then the pure spin current (1). In order to find Φ_2 , we calculated $\mathcal{J}_{z'}$ for the electrons with spins along z' axis and $\mathbf{e} \parallel x'$. To obtain Φ_1 , we assumed $e_{x'}, e_{z'} \neq 0$ and calculated $\mathcal{J}_{x'}$. Then, taking S in the form of Eq. (12), we get the electric current from Eq. (8). As a result, we obtain $j_{z'} = \Phi_2 B_{z'} e_{x'}^2 I$ and $j_{x'} = -\Phi_1 B_{z'} e_{x'} e_{z'} I$ in accordance with the phenomenological Eqs. (10), where $\Phi_1 = -\Phi_2$. Using the energy balance equation

$$\sum_{\mathbf{k}, \mathbf{k}', \pm} W_{\mathbf{k}'\mathbf{k}}^{(\pm)} (\varepsilon_{\mathbf{k}'} - \varepsilon_{\mathbf{k}}) = \alpha I, \quad (16)$$

where α is the absorption coefficient, we obtain the following estimate

$$|\Phi_{1,2}| \approx \xi \frac{e\tau m g \mu_B}{\hbar^3} \alpha. \quad (17)$$

Here m is the effective mass for parabolic dispersion, and $m = \varepsilon_F / v_0^2$ for a linear dispersion.

For the intraband absorption considered here, we can rewrite the obtained expression as follows

$$|\Phi_{1,2}| I \approx \xi \frac{N e^3 g \mu_B}{\hbar^3 \omega^2} |\mathbf{E}|^2, \quad (18)$$

where N is the electron concentration. Here we took into account that, in the conditions of the experiment $\omega\tau \gg 1$, and the absorption coefficient $\alpha \propto 1/\tau$. We see that the amplitude of MPGE current is independent of τ , so it is determined only by the electron concentration and radiation frequency.

In stronger classical magnetic fields, the asymmetric spin-dependent scattering Eq. (2) also results in the MPGE current. Accounting for the Lorentz force in the kinetic equation gives the results (10), (17) with the CR peak in the absorption coefficient [36]:

$$|\Phi_{1,2}| I \approx \xi \frac{N e^3 g \mu_B / \hbar^3}{(\omega \mp \omega_c)^2 + 1/\tau^2} |\mathbf{E}|^2. \quad (19)$$

Here ω_c is the classical cyclotron frequency for the electrons at the Fermi energy, and the upper and lower sign

is for the active ($\mathbf{E} \perp \mathbf{B}$) and passive ($\mathbf{E} \parallel \mathbf{B}$) linear polarizations in the Voigt geometry.

We see that the amplitude of MPGE current $j_x \propto B_y \Phi_{1,2}$ has resonant and nonresonant parts. In the active linear polarization, the current has a maximum at CR.

B. Quantizing magnetic fields

In higher magnetic fields, when Landau quantization takes place, the asymmetrical part of the electron-phonon interaction Eq. (2) also results in the fluxes in the spin subbands and in the MPGE electric current. Here we consider strong magnetic fields assuming that a complete spin polarization is established. In this case, according to Eq. (8) at $S = -1/2$, the MPGE current has a value $\mathbf{j} = -2e\mathcal{J}$.

We also assume that $\hbar\omega < \Delta$, where Δ is the energy gap between neighboring Landau subbands, so both the initial and final states of optical transitions lie in the same Landau subband. In so strong magnetic fields, a free motion of the carriers is possible along the \mathbf{B} direction only. Under these conditions, the MPGE current $\mathbf{j} \parallel \mathbf{B}$ is suppressed. This follows from the form of the scattering matrix element in Eq. (4), where at $\mathbf{k}, \mathbf{k}' \parallel \mathbf{B} \parallel y$ the term with σ_y is absent. Analogously, as can be seen from the corresponding Eq. (9), the orbital mechanism of MPGE also does not give a current $\mathbf{j} \parallel \mathbf{B}$ for any direction of \mathbf{B} .

The electric current perpendicular to \mathbf{B} is nonzero in quantized magnetic fields. It is formed due to shifts of the center of the cyclotron orbit of photoexcited electrons which occur at scattering by phonons [37], see Fig. 13. The direction of the shifts in the spin subbands is fixed by the odd in momentum terms in the probability of the electron-phonon interaction, Eq. (4).

In the nonresonant case, the radiation absorption is accompanied by phonon scattering. Therefore the shift current is formed in the process of absorption, Fig. 13(a). By contrast, at resonant absorption, carriers make direct optical transitions between the Landau subbands. The electric current $\mathbf{j} \perp \mathbf{B}$ may appear due to a shift of the carrier cyclotron orbit center in the final state in comparison to the initial state of the transition. However, at direct optical transitions such shifts equal to zero. This is clear if one takes the Landau gauge with the vector potential $A_z = -xB_y$, so the the cyclotron orbit center position is $k_z l_B^2$, where k_z is the wavevector of motion in the plane perpendicular to \mathbf{B} , and $l_B = \sqrt{\hbar/|eB|}$ is the magnetic length. The matrix element of a direct transition keeps k_z intact, therefore the shift of the cyclotron orbit center is absent [38]. The perpendicular to \mathbf{B} electric current is formed in the process of energy relaxation which follows the direct optical absorption process [37]. Fast inter-particle scattering establishes a quasi-equilibrium distribution with a temperature higher than the temperature of the lattice. Then this distribution relaxes via interaction with phonons. At scattering by phonons, the

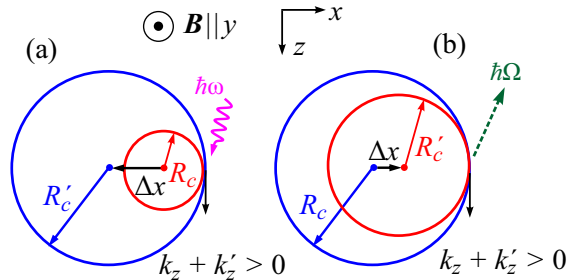


FIG. 13. Model of the perpendicular to the magnetic field electron flux in one spin subband in the classically strong magnetic field. Circles depict the cyclotron orbits in the (zx) plane perpendicular to the magnetic field $\mathbf{B} \parallel y$ for the particle with the cyclotron radius R_c . Blue and red circles depict cyclotron orbits for the carriers with higher and lower energy. Allowance for the wavevector-dependent contribution in Eq. (4) makes the electron-phonon scattering with $k_z + k'_z > 0$ more probable giving rise to the carrier flow in the given spin-up subband directed along x axis. Panel (a): The shift current formed at nonresonant radiation absorption. Red and blue circles depict cyclotron orbits for the electron before and after absorption of a photon with energy $\hbar\omega$ accompanied by a scattering on a phonon. Due to change of the cyclotron radius, the carrier shifts in the real space by $\Delta x = |R_c - R'_c|$, where R'_c is the cyclotron radius after the absorption process. Panel (b): The current formed at cooling of carriers by emission of phonons following a resonant radiation absorption. Blue and red circles depict cyclotron orbits for the electron before and after emission of a phonon with energy $\hbar\Omega$. Due to change of the cyclotron radius, the carrier shifts in the real space by $\Delta x = |R_c - R'_c|$, where R'_c is the cyclotron radius after the phonon emission.

electron cyclotron orbit center is shifted, Fig. 13(b).

Below we estimate the shift photocurrent $\mathbf{j} \perp \mathbf{B}$ for nonresonant intraband absorption and resonant CR and R transitions.

1. Nonresonant photocurrent

In the nonresonant case, the spin fluxes in the x direction read [37]

$$i_{x,s} = \sum_{\mathbf{k}, \mathbf{k}'} (x_{\mathbf{k}} - x_{\mathbf{k}'}) W_{\mathbf{k}'\mathbf{k}}^s, \quad (20)$$

where $x_{\mathbf{k}} = k_z l_B^2$ is cyclotron orbit center, and $W_{\mathbf{k}'\mathbf{k}}^s$ is the scattering assisted intraband optical absorption probability given by Eq. (15). This spin flux formation is illustrated in Fig. 13(a). If the Fermi energy exceeds by far the cyclotron energy, then one can ignore an effect of magnetic field on the electron scattering and use the above expression for calculation of the spin fluxes expressing all the values via the quantum numbers in the magnetic field [39]. Using the energy balance Eq. (16),

we obtain the following estimate for the electric current

$$j_x = e(i_{x,+} + i_{x,-}) \approx e\xi\tilde{k}^2 \sin 2\theta \sin \varphi_B \frac{\alpha I}{\hbar\omega_c}. \quad (21)$$

Here we again assumed a complete spin polarization, and \tilde{k} is a value of the mean wavevector corresponding to the Fermi energy or $k_B T$ at degenerate statistics and in the Boltzmann gas, respectively. Deriving Eq. (21), we took into account that the coefficients a_{ijl} introduced in Eq. (4) satisfy the relation $a_{zzz} + a_{zxx} + a_{zyy} = \sin 2\theta \sin \varphi_B$.

The obtained estimate of j_x , Eq. (21), is valid for any polarization of the absorbed radiation. The dependence of j_x on the polarization vector \mathbf{e} is present in Eq. (21) in the absorption coefficient $\alpha(\mathbf{e})$. The nonresonant absorption in a quantized magnetic field is different for polarizations along and perpendicular to \mathbf{B} . For $\mathbf{E} \parallel \mathbf{B}$, the energy absorption rate in the ground Landau subband is given by a usual high-frequency Drude expression

$$\alpha_{\parallel} I = 2|\mathbf{E}|^2 \frac{Ne^2}{m\omega^2\tau}. \quad (22)$$

For the configuration $\mathbf{E} \perp \mathbf{B}$, the electron-photon interaction has matrix elements between the neighboring Landau subbands only. Therefore, the radiation is absorbed due to virtual transitions via the next Landau subband. The absorbed power is given by

$$\alpha_{\perp} I = \hbar\omega \sum_{k,k'} W_{k'k}, \quad (23)$$

where k, k' are wavevectors in the magnetic field direction, and the probability of the optical transition $k \rightarrow k'$ is given by the Fermi Golden rule

$$W_{k'k} = \frac{2\pi}{\hbar} \sum_{\nu=\pm} [f_k(1-f_{k'})N_{\nu} - f_{k'}(1-f_k)N_{-\nu}] \times \left| (\tilde{U}_{k'k} + \tilde{U}_{kk'}) \frac{V_{n+1,n}}{\Delta} \right|^2 \delta(\varepsilon_k + \hbar\omega - \nu\hbar\Omega - \varepsilon_{k'}). \quad (24)$$

Here $\tilde{U}_{k'k}$ are matrix elements of intersubband scattering by phonons, $V_{n+1,n}$ and Δ are the electron-photon interaction matrix element and the energy gap between the Landau subbands with numbers n and $n+1$, and other notations are the same as in Eq. (15).

For parabolic energy dispersion we have

$$\Delta = \hbar\omega_c, \quad V_{n+1,n} = \frac{ie}{\omega} E \frac{\hbar\sqrt{n+1}}{\sqrt{2}ml_B}. \quad (25)$$

As a result, assuming $\hbar\omega \ll k_B T$ and $n = \varepsilon_F/\hbar\omega_c \gg 1$, we obtain

$$\alpha_{\perp} I = 4|\mathbf{E}|^2 \frac{Ne^2}{m\omega_c^2\tau} \left| \frac{\tilde{U}}{U} \right|^2, \quad (26)$$

where the last factor is a squared ratio of the inter- to intrasubband electron-phonon interaction matrix elements. A similar expression is valid for linear dispersion as well.

It follows from Eqs. (21) and (26) that the nonresonant photocurrent $j_x(\mathbf{E} \perp \mathbf{B})$ decreases in high magnetic fields according to

$$j_x(\mathbf{E} \perp \mathbf{B}) \sim \frac{1}{B^3}. \quad (27)$$

Since it is linear in B in low fields, Eq. (11), we conclude that it has a maximum as a function of B .

2. Resonant MPGE

The shifts of the cyclotron orbit center of resonantly heated carriers occur at their cooling which is carried out via scattering by phonons. The direction of the shifts is opposite in two spin subbands and dictated by the odd in momentum spin-dependent terms in the probability of the electron-phonon interaction. It follows from Eq. (4) that the latter has the form

$$\mathcal{W}_{\mathbf{k}'\mathbf{k}}^{\pm} = \mathcal{W}_0 \left(1 \pm 2\xi \sum_{i,j,l=x,y,z} a_{ijl} K_i K_j K_l \right), \quad (28)$$

where \mathcal{W}_0 is the probability of electron scattering by phonons without account for the non-centrosymmetry of the crystal.

The spin fluxes in the x direction read

$$i_{x,s} = \sum_{\mathbf{k},\mathbf{k}'} (x_{\mathbf{k}} - x_{\mathbf{k}'}) \mathcal{W}_{\mathbf{k}'\mathbf{k}}^s. \quad (29)$$

For carriers' energy relaxation by phonons following the resonant radiation absorption, the energy balance equation reads

$$\sum_{\mathbf{k},\mathbf{k}'} (\varepsilon_{\mathbf{k}} - \varepsilon_{\mathbf{k}'}) \mathcal{W}_0 = \alpha_{\text{res}} I, \quad (30)$$

where α_{res} is the resonant absorption coefficient. Then we obtain the following estimate for the electric current $j_x = e(i_{x,+} + i_{x,-})$

$$j_x \approx e\xi\tilde{k}^2 \sin 2\theta \sin \varphi_B \frac{\alpha_{\text{res}}(\omega) I}{\hbar\omega_c}. \quad (31)$$

Here we again assumed a complete spin polarization, and \tilde{k} is defined after Eq. (21). This expression shows that the resonant photocurrent has the same frequency dependence as the absorption coefficient. It is remarkable that this expression, despite being similar to Eq. (21) describing the MPGE current formed in the course of radiation absorption, differs strongly because here $\alpha_{\text{res}}(\omega)$ is the resonant absorption coefficient of a direct optical transition. A difference in microscopics of these two shift current formation is shown in Fig. 13.

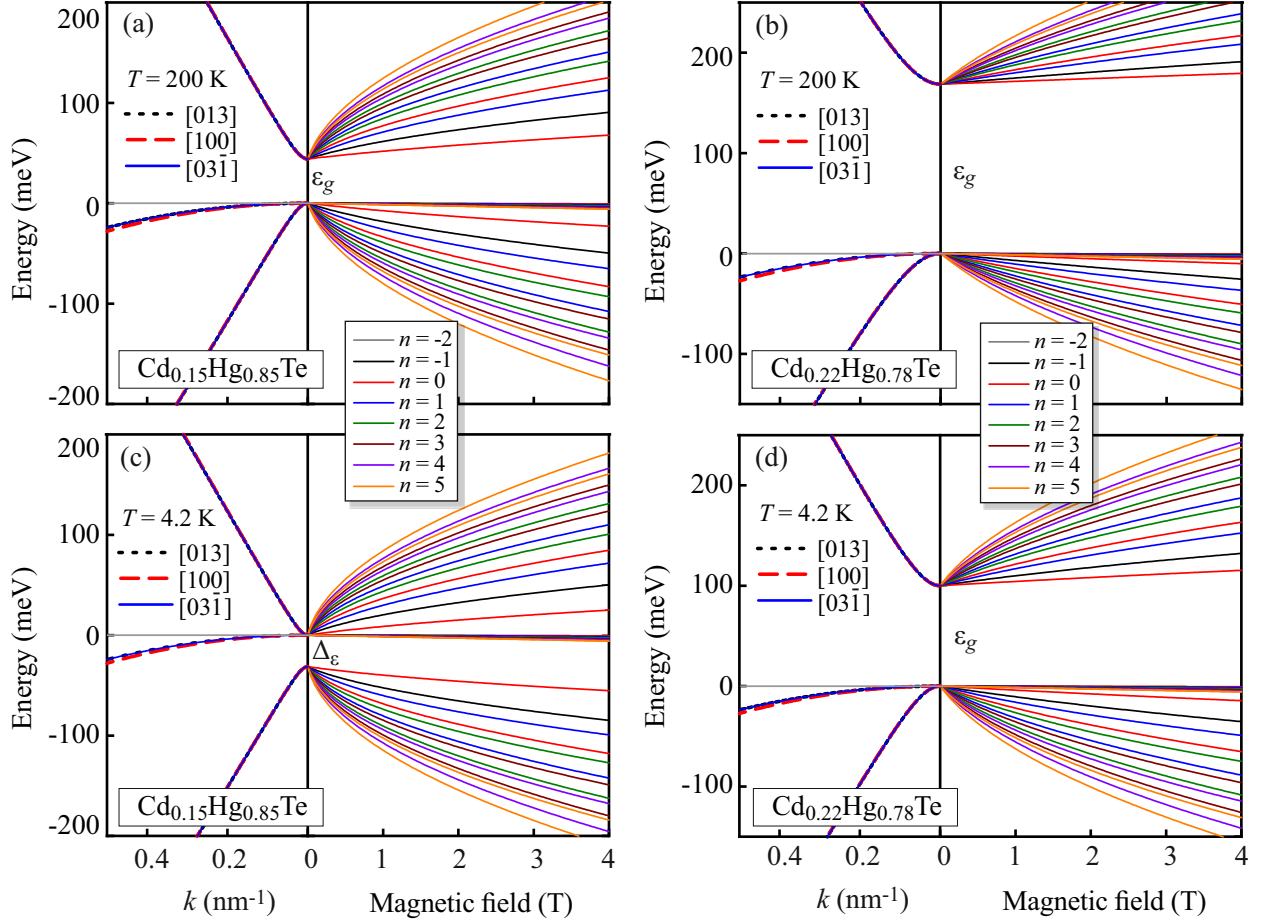


FIG. 14. Energy spectra of $\text{Cd}_x\text{Hg}_{1-x}\text{Te}$ with $x = 0.15$ and 0.22 calculated for $T = 200$ and 4.2 K. Left parts of each panel present the spectra at zero magnetic field. Here, ϵ_g is the band-gap of the bulk film, while Δ_ϵ represents the energy gap between Γ_6 and Γ_8 bands at the Γ point of the Brillouin zone. Note that $\text{Cd}_{0.15}\text{Hg}_{0.85}\text{Te}$ has $\epsilon_g = 0$ at $T = 4.2$ K, panel (c). Right parts show magnetic field dependencies of the Landau levels.

V. DISCUSSION

A. Nonresonant MPGE

The theory presented above explains our experimental findings described in Sec. III, including the origin of the nonresonant and resonant MPGE currents, the photocurrent behavior upon variation of the magnetic field, as well as its polarization and frequency dependencies.

At high temperatures, the resonant MPGE is not detected and the photoresponse is caused by the nonresonant MPGE in the whole range of magnetic fields. At low B , the photocurrent has opposite directions for $\pm B$ and increases linearly with increasing magnetic field, see Figs. 2 and 7, and radiation intensity, as it is expected from Eqs. (10), (11). The observed polarization dependence, see Figs. 3 and 9, is also in line with the theory. In the experiments, the angle α defining the polarization state was reckoned from the x axis in the sample plane which is perpendicular to \mathbf{B} , Fig. 12. In two samples under study, the angle between \mathbf{B} and the [100] axis is

$\varphi_B \approx \pm 45^\circ$, see Fig. 12. Therefore we have from Eq. (11)

$$j_\perp = \pm \frac{B \cos 2\theta}{2} (\Phi_1 \cos 2\alpha - \Phi_2) I, \quad (32)$$

where the upper and lower signs are for samples A and B, respectively, where signals by chance were picked up along two perpendicular crystallographic directions. We see that in both cases the current j_\perp contains the polarization independent part and the part depending on the radiation polarization as $\propto \cos 2\alpha$, as detected in experiment, see Figs. 3 and 9.

Figures 2 and 3 demonstrate that the photocurrent excited by radiation with lower frequency ($f = 0.6$ THz) is about 4 times smaller than that in response to the radiation with $f = 1.07$ THz. This difference follows from Eq. (18) which yields for the frequency dependence of the MPGE current $j \propto \omega^{-2}$.

At low temperatures and low magnetic field the nonresonant MPGE is hidden by a much stronger resonant MPGE, see Figs. 4, 5, 6, 8, and 10. However, it is clearly detected at high magnetic fields and for some frequen-

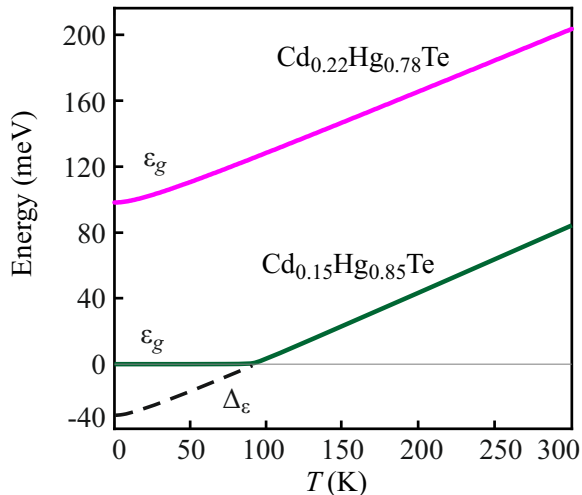


FIG. 15. Calculated temperature dependence of the band gap ε_g , and the energy gap Δ_ε between Γ_6 and Γ_8 bands at the Γ point of the Brillouin zone in $\text{Cd}_x\text{Hg}_{1-x}\text{Te}$ with $x = 0.15$ and 0.22 .

cies shows up as raising nonresonant photoresponse at low magnetic fields, too. In contrast to the low magnetic field regime, at high magnetic field it decreases upon the magnetic field increase, which is also in agreement with the theory. It follows from Eqs. (11) and (27) that $j_x(\mathbf{E} \perp \mathbf{B})$ raises linearly at low fields and drops as $1/B^3$ at high fields. This allows one to approximate the whole magnetic-field dependence of the nonresonant part by an empirical formula

$$j_x = \frac{aB}{cB^4 + d}. \quad (33)$$

The corresponding fits are presented in Figs. 4. The decrease of the signal at high fields is also detected at high temperatures, however, it is not only decreases with raising B , but even changes its sign, see Figs. 2 and 7. We attribute this fact to the interplay of the spin and orbital mechanisms of the MPGE, see Eqs. (2) and (9), which give opposite signs of the photocurrent, and approach maximum at different magnetic field values.

B. Resonant MPGE

1. CR induced MPGE in sample with $x = 0.15$

We begin with the discussion of the resonant MPGE detected in sample A with $x = 0.15$, see Figs. 4, 5, and 6. Natural candidates for the resonant MPGE are the photocurrents caused by the cyclotron resonance (CR) and inter Landau level transitions. In the Voigt geometry used in our experiments the CR can only be excited if the radiation electric field is oriented normally to the magnetic field, $\mathbf{E}(\omega) \perp \mathbf{B}$. These conditions fulfill the resonances labeled as CR in Figs. 5 and 6. To confirm this

TABLE I. Resonance positions and the cyclotron mass m_{CR} obtained for sample A.

Data for $\text{Cd}_{0.15}\text{Hg}_{0.85}\text{Te}$								
		Resonance position, mT						
$\hbar\omega$, meV	λ , μm	CR	R_1	R_2	R_3	R_4	R_5	CR mass, m_{CR}/m_0
13.7	90	430	100	190	250	330	560	0.0036
8.4	148	265	85	100	133	180	290	0.0036
4.4	280	115	39	48	64	140	–	0.0031
2.5	496	60	33	45	82	–	–	0.0028

conclusion and to identify multiple R-type resonances we calculated the energy dispersion of $\text{Cd}_{0.15}\text{Hg}_{0.85}\text{Te}$ and analyzed possible optical transitions for all frequencies used in our experiments, see Figs. 14, 15, and 16.

TABLE II. Resonance positions and the cyclotron mass m_{CR} obtained for sample B.

Data for $\text{Cd}_{0.22}\text{Hg}_{0.78}\text{Te}$					
		Resonance position, mT			
$\hbar\omega$, meV	λ , μm	CR	\mathcal{R}		CR mass, m_{CR}/m_0
13.7	90	1140	–		0.0095
8.4	148	630	125		0.0086
4.4	280	300	290		0.0078
2.5	496	145	620		0.0067

Figures 14 and 16 show the band structure and Landau levels (LLs) calculated using the eight-band $\mathbf{k} \cdot \mathbf{p}$ Kane Hamiltonian, which directly takes into account the interactions between Γ_6 , Γ_8 , and Γ_7 bands (neglecting the contribution due to the bulk inversion asymmetry). To calculate the energy of LLs, we apply the axial approximation by omitting the warping terms in the Hamiltonian. In this case, the electron-wave function for a given LL index $n > 0$ generally has eight components, describing the contribution of the Γ_6 , Γ_8 , and Γ_7 bands into the LL. We note that a specific LL with $n = -2$ contains only a contribution of the heavy-hole band with a momentum projection $\pm 3/2$. Details of the LL notation, explicit form of the Hamiltonian and temperature dependent band-structure parameters are provided in Ref. [40].

The observed resonances in the MPGE current are described by Eq. (31), which shows that the photocurrent is proportional to the absorption coefficient and, therefore, follows to the absorption Lorentzian, see Figs. 6. As next we read out from the experiment plots positions of the polarization dependent resonances labeled as CR and depicted them in Fig. 16 by vertical lines with the length corresponding to used photon energies. Figures 16(b)-(d) show that for radiation frequencies $f = 1.07$ THz ($\hbar\omega = 4.4$ meV), 2.03 THz ($\hbar\omega = 8.4$ meV), and 3.33 THz ($\hbar\omega = 13.7$ meV) the corresponding arrows perfectly fit transitions between the zeroth and the first Kane fermion LLs in the conduction band, i.e. indeed correspond to the CR. Note that for $f = 0.6$ THz ($\hbar\omega = 2.5$ meV) the CR

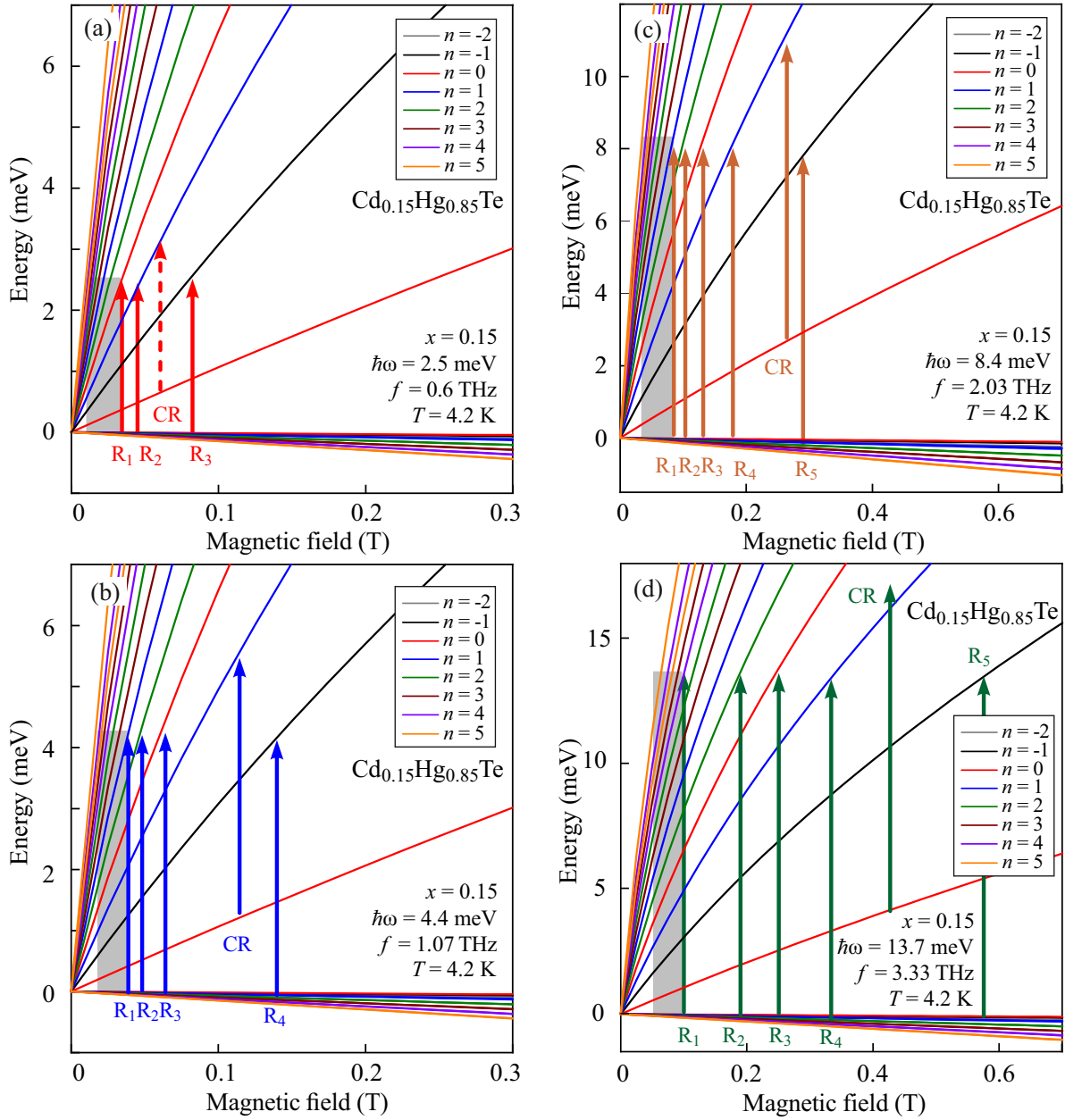


FIG. 16. Zoom of the low energy part of magnetic field dependence of the Landau levels for $\text{Cd}_x\text{Hg}_{1-x}\text{Te}$ with $x = 0.15$ calculated for $T = 4.2$ K. Vertical arrows show resonant optical transitions detected in experiment, see Fig. 6. The arrows are labeled as CR and $R_{1,2,3,4,5}$ which depict the polarization sensitive and polarization independent resonances, respectively. The length of the arrows corresponds to the photon energies used in our experiments: $f = 0.6$ THz ($\hbar\omega = 2.5$ meV), $f = 1.07$ THz ($\hbar\omega = 4.4$ meV), 2.03 THz ($\hbar\omega = 8.4$ meV), and 3.33 THz ($\hbar\omega = 13.7$ meV). Gray rectangles sketch possible optical transitions involving high LLs, which can hardly be resolved in our experiments. For the magnetic fields that correspond to the sketched resonances, see Table I.

resonance position is very close to the polarization independent R-resonance, which could be the reason why it was not resolved in our experiments, see dashed arrow in Fig. 16(a).

Electron cyclotron mass and the lowest limit of the momentum relaxation time can be estimated from the resonance position and the full width half maximum (FWHM), see Figs. 5, 16 and the inset in Fig. 10. We ob-

tained the CR mass increases with raising frequency from $0.032 m_0$ ($f = 1.06$ THz) to $0.0035 m_0$ ($f = 3.33$ THz), see Table I, and that the momentum relaxation time is longer or equal to 0.5 ps. Note that the resonances can be broadened by interference effects or superradiant decay [41–45]. The obtained values confirm that the resonances are caused by the optical transitions in the conduction band and are in agreement with the transport

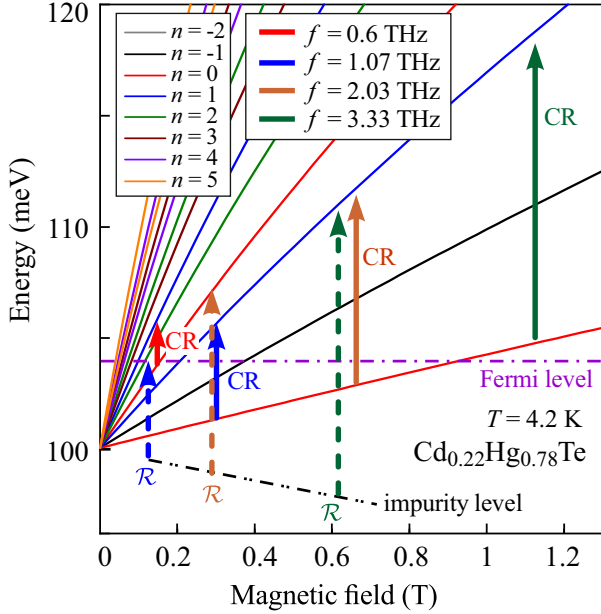


FIG. 17. Zoom of the low energy part of magnetic field dependence of the Landau levels for $\text{Cd}_x\text{Hg}_{1-x}\text{Te}$ with $x = 0.22$ calculated for $T = 4.2$ K. Vertical arrows show resonant optical transitions detected in experiment, see Fig. 10. For the corresponding magnetic fields see Table II. The arrows are labeled as CR and \mathcal{R} , which depict the polarization sensitive and polarization independent resonances, respectively. The length of the arrows corresponds to the photon energies used in our experiments: $f = 0.6$ THz ($\hbar\omega = 2.5$ meV); $f = 1.07$ THz ($\hbar\omega = 4.4$ meV); 2.03 THz ($\hbar\omega = 8.4$ meV), and 3.33 THz ($\hbar\omega = 13.7$ meV).

data for electrons, see Appendix A.

We would like to emphasize that, at low temperatures, the magnitude of the resonant and even non-resonant magneto-photogalvanic current J/P is enormously large approaching several milliAmperes per Watt, see, e.g. Fig. 4. To our knowledge it exceeds THz-radiation induced photogalvanic currents in other materials by several orders of magnitude.

2. \mathcal{R} -type resonant MPGE in sample with $x = 0.15$

Now we turn to the polarization independent resonances of type R. Figure 14 shows that the photon energies used in our experiments may result in the interband transitions, because $\text{Cd}_{0.15}\text{Hg}_{0.85}\text{Te}$ has zero band-gap at $T = 4.2$ K, see Fig. 15. Note that the energy gap between Γ_6 and Γ_8 bands at the Γ point is about 40 meV, see Fig. 14, that exceeds significantly our photon energies $\hbar\omega \leq 13.7$ meV.

Alike for the CR resonances we depicted in Fig. 16 all detected R-resonances by vertical arrows with the length corresponding to used photon energies. One can see that all optical transitions start in the valence band and have final states on one of the electron LLs. We emphasize

that those resonances in the terahertz range of frequencies are only possible for Kane fermion energy dispersion resulting in the almost flat valence band and, for $x = 0.15$ and low temperatures, in zero band gap. Previously these transitions have been detected in experiments on the radiation transmission [46]. Importantly, according to the selection rules such resonances are allowed in any polarization, see Refs. [1, 21] and Sec. IV B 2, which completely agrees with experiment. Also in line with experiment the observed resonances in the MPGE current are described by Eq. (31), and consequently, the photocurrent is proportional to the absorption coefficient having a Lorentzian shape, see Fig. 6. Figure 6 also reveals that the amplitude of the R-resonances are substantially larger than that of the CR one. This observation we attribute to the higher populations of the initial states for R transitions than for CR.

To finalize the discussion of the resonances in $\text{Cd}_{0.15}\text{Hg}_{0.85}\text{Te}$ at $T = 4.2$ K we note that, despite under these conditions the film is characterized by the inverted band structure, we did not find any traces of the MPGE involving Pankratov-Volkov surface states. This conclusion can be reached because the photocurrent response of two samples with normal and reverse banding does not differ qualitatively.

3. CR- and \mathcal{R} -type resonant MPGE in sample with $x = 0.22$

As next we discuss the resonances detected at $T = 4.2$ K in $\text{Cd}_{0.22}\text{Hg}_{0.78}\text{Te}$, see Figs. 8 and 10, applying the same procedure as we used for the analysis of the resonances in $\text{Cd}_{0.15}\text{Hg}_{0.85}\text{Te}$. The results are shown in Fig. 17 in which a color code is used to highlight optical transitions excited by the radiation with different photon energies shown by vertical arrows. First of all the polarization dependent resonant MPGE currents in Figs. 8 and the resonances labeled as CR in Fig. 10(a) (red arrow), correspond well to the transitions between the 0th and 1st Kane fermion LLs in the conduction band for all four frequencies. The CR electron mass determined from the resonance position monotonic increases with the frequency increase from $m = 0.0067m_0$ ($f = 0.6$ THz) to $0.0095m_0$ ($f = 3.33$ THz), see Table II. The lowest limit of the momentum relaxation time estimated from the FWHM is 1.1 ps. While also in this sample we detected the polarization independent resonances, they can not be attributed to the transitions between the LLs in the valence and conduction bands. As it is seen from Figs. 14 and 15, the band gap in this sample at $T = 4.2$ K is about 100 meV being much larger than any of photon energies used in our experiment. In contrast to the multiple R-resonances in $\text{Cd}_{0.15}\text{Hg}_{0.85}\text{Te}$, in $\text{Cd}_{0.22}\text{Hg}_{0.78}\text{Te}$ we detected only a single \mathcal{R} -lines for each frequency. Note that the maximum value of the \mathcal{R} -resonant photocurrent at the same frequency in the sample B is 4-5 times smaller than R-resonance in sample A. We attributed these res-

onances to the optical transitions from an impurity level to the first LL, see vertical arrows labeled by \mathcal{R} in Fig. 17, which were previously discussed in Ref. [47]. The shape of the photocurrent resonances also reflects the one of the absorption due to the direct optical transitions, see Eq. (31).

Finally we note, that the samples under study have a lower symmetry than T_d point group of an ideal bulk crystal. This follows from Ref. [18] where the helicity-dependent photocurrent was detected in the same samples. Microscopically, it is caused by additional compared to Eq. (2) terms in the electron-phonon interaction, which may result in the photocurrent contributions forbidden in T_d symmetry, e.g., the circular MPGE, which, however, are out of scope of the present study.

VI. SUMMARY

Our studies show that irradiation of $\text{Cd}_x\text{Hg}_{1-x}\text{Te}$ crystals hosting Kane fermions with THz radiation leads to magnetophotogalvanic currents with the magnitude, to our knowledge, is orders of magnitude that larger than those studied in other systems. By measuring the MPGE current at room and liquid helium temperatures in crystals with different values of Cd content x we observed nonresonant and resonant photocurrents. The developed theory, which considers a pure spin current excited by asymmetric spin-dependent scattering and converted into a dc electric current by the Zeeman effect, explains the experimental results well. The nonresonant MPGE is shown to be caused by Drude absorption assisted by phonon scattering. All the resonances observed at low temperature in the MPGE current are well described by optical transitions between the adjusting conduction band Landau levels (CR-resonance), interband transitions from the valence band to the higher LL (R-resonances, samples with Cd content $x = 0.15$), and optical transitions from the impurity level of the higher LL levels (\mathcal{R} -resonances, samples with Cd content $x = 0.22$). The positions of the CR and multiple R-type resonances surprisingly well correspond to the band structure and LL position calculated using the eight-band $\mathbf{k} \cdot \mathbf{p}$ Kane Hamiltonian, which directly accounts for the interactions between the Γ_6 , Γ_8 , and Γ_7 bands.

VII. ACKNOWLEDGMENTS

We thank I. Yachniuk for fruitful discussions. The financial support of the Deutsche Forschungsgemeinschaft (DFG, German Research Foundation) via Project-ID 521083032 (Ga501/19), the Volkswagen Stiftung Program (97738) is gratefully acknowledged. We also acknowledge the France 2030 program for Equipex+ HYBAT project (ANR-21-ESRE-0026), the Physics Institute of CNRS for Tremplin 2024 - STEP - project, the Occitanie Region for the “Quantum Technologies Key

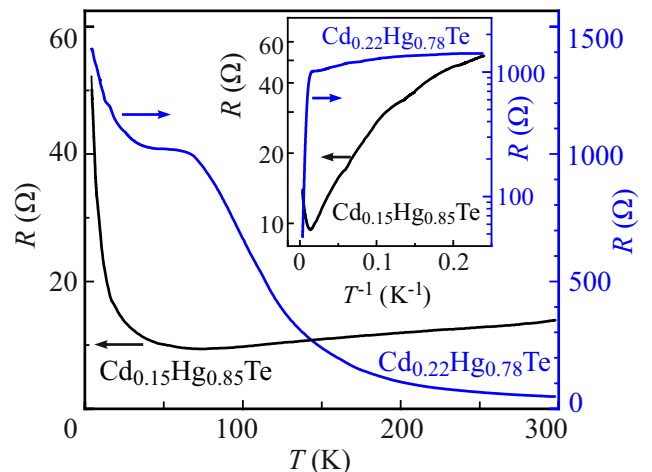


FIG. A.1. Temperature dependence of the two-point resistance measured in samples A (black, left axis) and B (blue, right axis). Inset shows the data re-plotted as Arrhenius plot.

Challenge” program - TARFEP - project, and the Terahertz Occitanie Platform.

Appendix A: Analysis of the transport and magnetotransport data obtained for $\text{Cd}_x\text{Hg}_{1-x}\text{Te}$ with $x = 0.15$ and 0.22 .

The MPGE studies were supplemented by transport measurements performed both on samples A and B and on other samples made of the same substrates (hereinafter referred to as samples A_1 and B_1). The dependences of $R(T)$ in zero magnetic field and at temperatures from 4.2 to 300 K presented in Fig. A.1 show that the resistance of sample A_1 varies in the range from 10 to 50 Ohm, and for sample B_1 from 50 to 1500 Ohm. Despite more than an order of magnitude difference in resistance, the behavior of the samples remains similar. For both investigated samples, the course of the temperature dependence of the resistance is mainly determined by the processes of charge carrier activation as well as phonon scattering. At low temperature, the resistance of both samples saturates at values of 50 and 1500 Ohm, which is characteristic of metallic or semi-metallic systems. Together with the large value of the band gap at $T = 0$ for sample B_1 (≈ 100 meV, see Fig. 15), this indicates a banded zone structure along the z -axis, probably arising during the process of film growth, and forming spatially separated electronic and hole layers, degenerated at low temperatures. For sample A_1 , band bending is also possible, but not necessary, since the effective value of the energy gap, which determines the activation of carriers, is equal to 0 for the inverted spectrum. The resistance of the sample B_1 decreases with temperature with two characteristic regions (weakly at low T , and then sharply at high T , see the inset in Fig. A.1, where the $\ln R(1/T)$ dependences are shown), which may be related

to the transition from the degenerate to the nondegenerate state. In this case, the crossover temperature (80 K) should coincide in order of magnitude with the electron Fermi energy, which allows us to estimate it as 7 meV. By contrast, for sample A_1 there is no pronounced activation dependence at any temperature, instead there is a broad minimum of resistance between 50 and 100 K. This behavior of $R(T)$ reflects the strong dependence of the band gap ε_g on temperature and its transition through zero, see Fig. 15.

To identify charge carriers and determine their parameters (density and mobility), magnetotransport measurements were carried out for samples A_1 and B_1 using a 4-point scheme in the temperature range from 100 mK to 150 K and in a magnetic field up to 10 T, see Fig. A.2(a) and (b). The obtained $\rho_{xx}(B)$ and $\rho_{xy}(B)$ dependencies were recalculated into conductivity tensor components $\sigma_{xx}(B)$ and $\sigma_{xy}(B)$ and fitted by the Drude model with multiple carrier types. For simplicity, we consider the system under study as two-dimensional system. This approach is justified in the absence of the current flow along the growth axis of the sample, which is fulfilled in samples of large size (i.e., with negligibly small edge effects) and in the absence of a magnetic field in the sample plane. Because of the significant reduction of $\sigma_{xx}(B)$ and $\sigma_{xy}(B)$ in a strong magnetic field (by almost 4 orders of magnitude relative to the maxima), a weight function was used that proportionally amplifies the contribution of asymptotically small σ_{xx} and σ_{xy} regions at high B . The fitting by several types of carriers was chosen for the following considerations: first, several types of carriers have been observed in thick HgTe quantum wells [48, 49] and HgTe and CdHgTe films [10, 21], and therefore similar behavior can be expected in the investigated bulk CdHgTe films. In this case, due to the lack of doping and the system's tendency to electroneutrality, the total density of electrons and holes should be comparable; secondly, the simultaneous existence of electrons and holes is indicated by the positive magnetoresistance and strongly nonlinear Hall resistance $\rho_{xy}(B)$, Fig. A.2(a) and (b). Fitting by the simplest model with one type of carriers in this case gives a meaningless result: the average slope of the $\rho_{xy}(B)$ dependence for the sample B_1 first increases with increasing temperature, which, using a one-component model, would mean a decrease in the carrier concentration, which contradicts the observed temperature dependence $R(T)$. When using the Drude model with two types of carriers (electrons and holes), the result becomes more plausible, but the addition of a third group of carriers (slow electrons) allows for even better agreement between the fit and experiment. An example of such fits for sample A_1 is shown in Fig. A.2(c) and (d).

When using the multicomponent Drude model, it is necessary to keep in mind its limitations associated with

the impossibility of separating carriers of close mobility and masking of low-mobility carriers due to their small contribution to the conductivity. Another important aspect is the incomplete correspondence between the model, which assumes independent groups of carriers with uniquely defined and independent of the magnetic field parameters, and the real system. Therefore, the use of even three types of carriers is not always justified, and the transition to a continuum distribution (mobility spectrum approach [21]) turns out to be a deliberate excess of the model accuracy. The results of the fitting, taking into account the above factors, are presented in Figs. A.3 and A.4 for samples A_1 and B_1 , respectively.

The sample A_1 (Fig. A.3) at low temperature is characterized by two groups of electrons with equal concentration of about $1.6 \times 10^{11} \text{ cm}^{-2}$, but with different 2 orders of mobility (10^4 and $2 \times 10^6 \text{ cm}^2/\text{V}\cdot\text{s}$), as well as holes (with concentration $p_s = 3.6 \times 10^{11} \text{ cm}^{-2}$ and mobility $2000 \text{ cm}^2/\text{V}\cdot\text{s}$). The resulting densities are two-dimensional as they are naturally obtained by fitting the experimental data with the two-dimensional Drude model. To translate into three-dimensions, the thickness of the layer in which certain carriers are localized is required, the exact value of which remains unknown, thus, we present 2D densities. The values obtained are in qualitative agreement with recent Ref. [21], as well as the older work Ref. [50]. With increasing temperature, the mobility of low-mobility electrons decreases rapidly, but the reliability of the fit also decreases. At temperatures above 10 K, reliable separation of this group of electrons is not possible, and further fitting was performed using only one type of electrons and holes. For the same reason, the maximum of hole mobility is observed in this region, which is an artifact. The high-mobility electrons are apparently bulk carriers (rather than topological surface states) whose high mobility is associated with a low effective mass value. From the point of view of transport measurements, this is confirmed both by the absence of Shubnikov-de Haas oscillations at 80 mK (not shown) and by the preservation of mobility at high values up to $T = 150 \text{ K}$, i.e., above the temperature of transition to the normal spectrum.

The type B sample (Fig. A.4) is similarly characterized by two kinds of electrons and holes with densities of the same order ($n_1 = 1.6 \times 10^{11} \text{ cm}^{-2}$, $n_2 = 3.7 \times 10^{11} \text{ cm}^{-2}$ and $p_s = 6.2 \times 10^{11} \text{ cm}^{-2}$). In comparison to the type A sample, here all carriers are characterized by much lower mobility, not exceeding $10^5 \text{ cm}^2/\text{V}\cdot\text{s}$ for fast electrons, $4000 \text{ cm}^2/\text{V}\cdot\text{s}$ for slow electrons, and $1900 \text{ cm}^2/\text{V}\cdot\text{s}$ for holes. As the temperature increases, the mobility of low-mobility carriers decrease rapidly, which also reduces the reliability of the fit. At $T > 15 \text{ K}$, the mobility of holes becomes less than $1000 \text{ cm}^2/\text{V}\cdot\text{s}$, which makes further fit too inaccurate.

[1] M. Orlita, D. M. Basko, M. S. Zholudev, F. Teppe, W. Knap, V. I. Gavrilenko, N. N. Mikhailov, S. A.

Dvoretiskii, P. Neugebauer, C. Faugeras, A.-L. Barra,

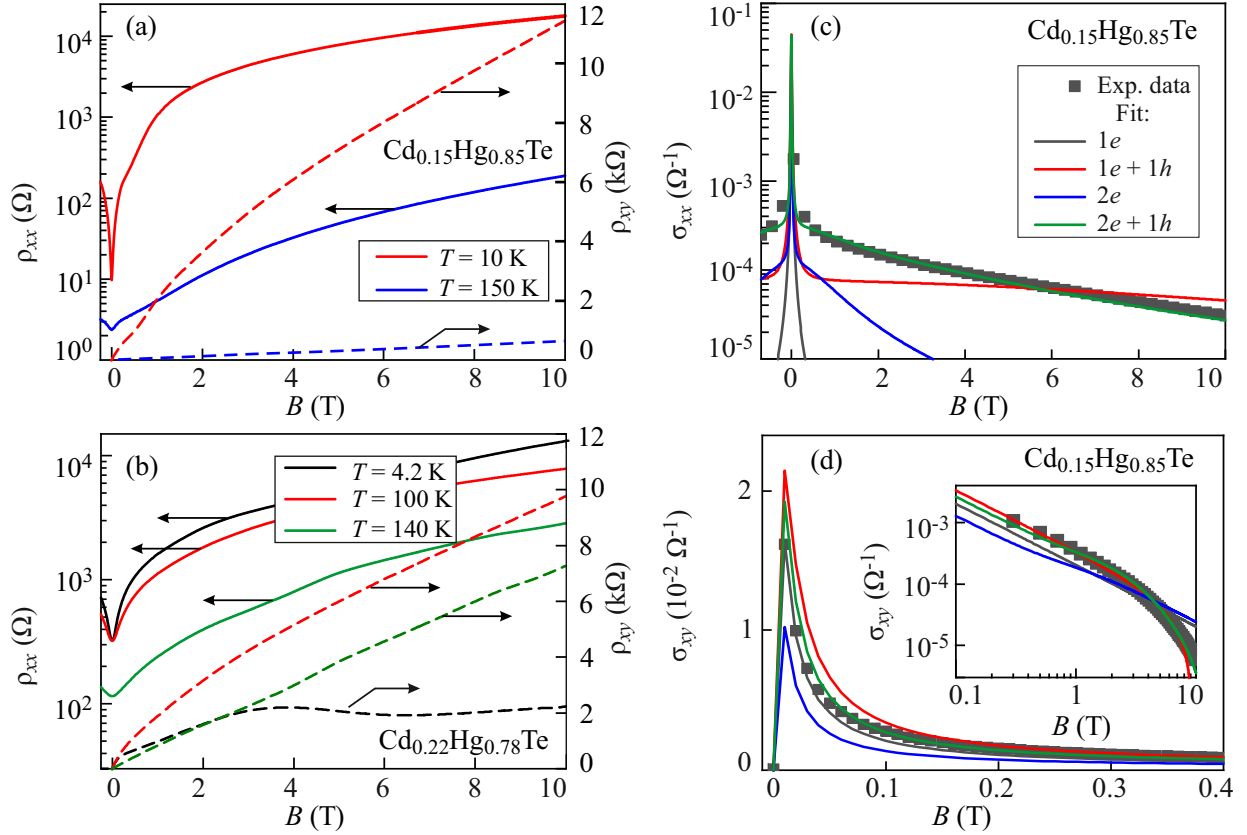


FIG. A.2. (a) and (b): experimental dependences $\rho_{xx}(B)$ (solid lines, left) and $\rho_{xy}(B)$ (dashed, right) for A and B samples, respectively, measured at low and high temperatures. (c) and (d): an example of the fitting of $\sigma_{xx}(B)$ and $\sigma_{xy}(B)$, respectively, by the Drude model with different amount of carrier groups. Experimental data are obtained from the $\rho_{xx}(B)$ and $\rho_{xy}(B)$ dependences for the sample A at a temperature of 1.6 K and are shown as separate points. The solid lines depict the different fits: one electron type (e, black), one electron and one hole group (e + h, red), two electron groups (2e, blue), and two electron and one hole groups (2e + 1h, green). It is well seen that the last fit follows the experimental data significantly better than all the others. The inset in panel (d) shows the dependences of $\sigma_{xy}(B)$ over a wider range of B and on a logarithmic scale.

- G. Martinez, and M. Potemski, Observation of three-dimensional massless kane fermions in a zinc-blende crystal, *Nature Physics* **10**, 233 (2014).
- [2] F. Tepe, M. Marcinkiewicz, S. S. Krishtopenko, S. Ruffenach, C. Consejo, A. M. Kadykov, W. Desrat, D. But, W. Knap, J. Ludwig, S. Moon, D. Smirnov, M. Orlita, Z. Jiang, S. V. Morozov, V. Gavrilenko, N. N. Mikhailov, and S. A. Dvoretzky, Temperature-driven massless kane fermions in hgcdte crystals, *Nature Communications* **7**, 10.1038/ncomms12576 (2016).
- [3] J. P. Laurenti, J. Camassel, A. Bouhemadou, B. Toulouse, R. Legros, and A. Lusson, Temperature dependence of the fundamental absorption edge of mercury cadmium telluride, *Journal of Applied Physics* **67**, 6454 (1990).
- [4] T. C. Harman, A. J. Strauss, D. H. Dickey, M. S. Dresselhaus, G. B. Wright, and J. G. Mavroides, Low electron effective masses and energy gap in $\text{Cd}_x\text{Hg}_{1-x}\text{Te}$, *Physical Review Letters* **7**, 403 (1961).
- [5] M. Szola, Y. Ivonyak, J. Przybytek, N. Mikhailov, S. Dvoretzky, F. Tepe, and W. Knap, Hydrostatic deformation potentials of narrow-gap hgcdte, *Physical Review B* **106**, 195202 (2022).
- [6] S. S. Krishtopenko, M. Antezza, and F. Tepe, Disorder-induced topological phase transition in hgcdte crystals, *Physical Review B* **106**, 115203 (2022).
- [7] O. Pankratov, S. Pakhomov, and B. Volkov, Supersymmetry in heterojunctions: Band-inverting contact on the basis of pb1-xsnxte and hg1-xcdxte, *Solid State Communications* **61**, 93 (1987).
- [8] S. S. Krishtopenko, M. Antezza, and F. Tepe, Hybridization of topological surface states with a flat band, *Journal of Physics: Condensed Matter* **32**, 165501 (2020).
- [9] A. S. Kazakov, A. V. Galeeva, A. I. Artamkin, A. V. Ikonnikov, L. I. Ryabova, S. A. Dvoretzky, N. N. Mikhailov, M. I. Bannikov, S. N. Danilov, and D. R. Khokhlov, Distinction between electron states formed at topological insulator interfaces with the trivial phase and vacuum, *Scientific Reports* **11**, 10.1038/s41598-021-91141-2 (2021).
- [10] M. L. Savchenko, D. A. Kozlov, N. N. Vasilev, N. N. Mikhailov, S. A. Dvoretzky, and Z. D. Kvon, Transport properties of a 1000 nm HgTe film: the interplay of surface and bulk carriers, *Journal of Physics: Condensed Matter* **35**, 345302 (2023).
- [11] A. Inhofer, S. Tchoumakov, B. A. Assaf, G. Fève, J. M. Berroir, V. Jouffrey, D. Carpentier, M. O. Goer-

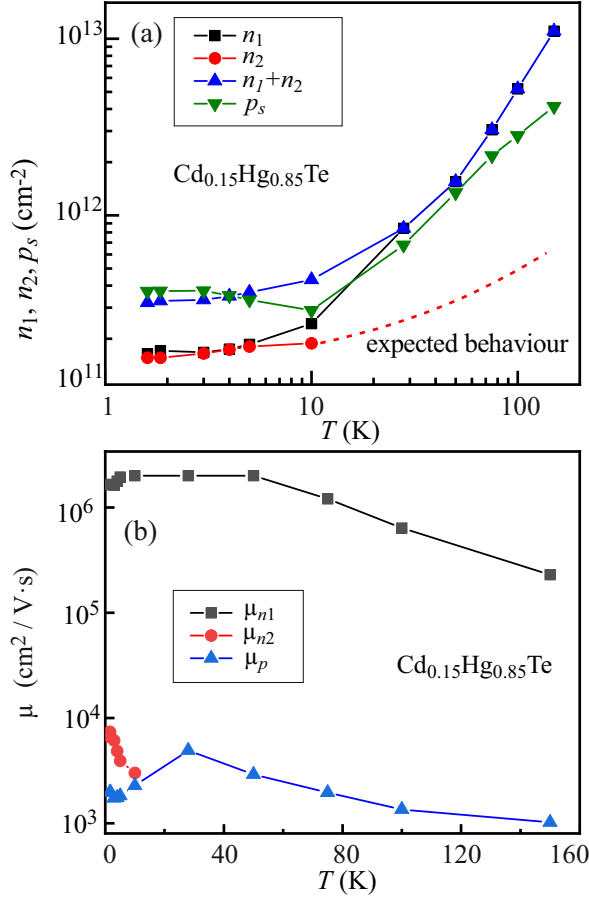


FIG. A.3. Carrier densities n and p (a) and mobility μ (b) for the sample A_1 extracted from the fit of magneto-transport data shown in Fig. A.2 applying 3-carriers Drude model. The model involves fast electrons (n_1), slow electrons (n_2) and holes (p). Note that at $T > 10$ K the mobility of slow electrons becomes so small, so it makes further reliable identification of these carriers impossible. Thus, the fit for higher T was made only for 2 types of carriers. In this aspect, the increase in mobility μ_p at $T = 25$ K must be considered as an artifact. The expected density dependence $n_{n2}(T)$ shown by a dashed red line.

big, B. Plaais, K. Bendias, D. M. Mahler, E. Bocquillon, R. Schlereth, C. Brune, H. Buhmann, and L. W. Molenkamp, Observation of volkov-pankratov states in topological hgte heterojunctions using high-frequency compressibility, *Physical Review B* **96**, 195104 (2017).

- [12] M. Otteneder, D. Sacre, I. Yahniuk, G. V. Budkin, K. Diendorfer, D. A. Kozlov, I. A. Dmitriev, N. N. Mikhailov, S. A. Dvoretzky, V. V. Bel'kov, W. Knap, and S. D. Ganichev, Terahertz magnetospectroscopy of cyclotron resonances from topological surface states in thick films of $\text{Cd}_x\text{Hg}_{1-x}\text{Te}$, *Phys. Status Solidi B* **258**, 2000023 (2020).
- [13] A. Akrap, M. Hakl, S. Tchoumakov, I. Crassee, J. Kuba, M. Goerbig, C. Homes, O. Caha, J. Novak, F. Tepe, W. Desrat, S. Koochpayeh, L. Wu, N. Armitage, A. Nateprov, E. Arushanov, Q. Gibson, R. Cava, D. van der Marel, B. Piot, C. Faugeras, G. Martinez, M. Potemski, and M. Orlita, Magneto-optical signature

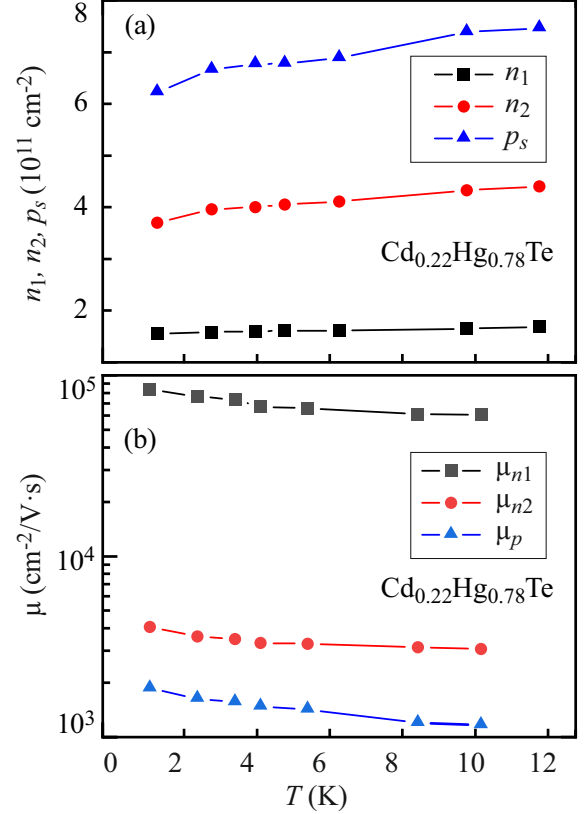


FIG. A.4. Carrier densities n and p (a) and mobility μ (b) for the sample B_1 extracted from the fit of magneto-transport data shown in Fig. A.2 applying 3-carriers Drude model. As for type A sample, the model involves fast electrons (n_1), slow electrons (n_2) and holes (p). At $T \geq 15$ K the hole mobility becomes smaller than $1000 \text{cm}^2/\text{V}\cdot\text{s}$, making the whole fitting unreliable.

of massless kane electrons in Cd_3As_2 , *Physical Review Letters* **117**, 136401 (2016).

- [14] S. S. Krishtopenko and F. Tepe, Relativistic collapse of landau levels of kane fermions in crossed electric and magnetic fields, *Physical Review B* **105**, 125203 (2022).
- [15] A. V. Galeeva, A. I. Artamkin, N. N. Mikhailov, S. A. Dvoretzskii, S. N. Danilov, L. I. Ryabova, and D. R. Khokhlov, Terahertz photoconductivity in $\text{Hg}_{1-x}\text{Cd}_x\text{Te}$ near the transition from the direct to inverted spectrum, *JETP Lett.* **106**, 162 (2017).
- [16] S. Ruffenach, A. Kadykov, V. V. Rumyantsev, J. Torres, D. Coquillat, D. But, S. S. Krishtopenko, C. Consejo, W. Knap, S. Winnerl, M. Helm, M. A. Fadeev, N. N. Mikhailov, S. A. Dvoretzskii, V. I. Gavrilenko, S. V. Morozov, and F. Tepe, HgCdTe-based heterostructures for terahertz photonics, *APL Mater.* **5**, 035503 (2017).
- [17] A. V. Galeeva, A. S. Kazakov, A. I. Artamkin, L. I. Ryabova, S. A. Dvoretzky, N. N. Mikhailov, M. I. Bannikov, S. N. Danilov, and D. R. Khokhlov, Apparent pt-symmetric terahertz photoconductivity in the topological phase of $\text{Hg}_{1-x}\text{Cd}_x\text{Te}$ -based structures, *Scientific Reports* **10**, 10.1038/s41598-020-59280-0 (2020).
- [18] S. Hubmann, G. V. Budkin, M. Otteneder, D. But, D. Sacre, I. Yahniuk, K. Diendorfer, V. V. Belkov, D. A.

- Kozlov, N. N. Mikhailov, S. A. Dvoretzky, V. S. Varavin, V. G. Remesnik, S. A. Tarasenko, W. Knap, and S. D. Ganichev, Symmetry breaking and circular photogalvanic effect in epitaxial cdhg films, *Physical Review Materials* **4**, 043607 (2020).
- [19] S. A. Dvoretzky, N. N. Mikhailov, D. G. Ikuov, V. A. Kartashev, A. V. Kolesnikov, I. V. Sabinina, Y. G. Sidorov, and V. A. Shvets, The growth of CdTe layer on GaAs substrate by MBE, in *Cadmium Telluride (CdTe) - Prospects, Challenges and Applications* (IntechOpen, 2019).
- [20] V. S. Varavin, S. A. Dvoretzky, N. N. Mikhailov, V. G. Remesnik, I. V. Sabinina, Y. G. Sidorov, V. A. Shvets, M. V. Yakushev, and A. V. Latyshev, Molecular beam epitaxy of cdhgte: Current state and horizons, *Optoelectronics, Instrumentation and Data Processing* **56**, 456 (2020).
- [21] D. Yavorskiy, K. Karpierz, M. Baj, M. M. Bak, N. N. Mikhailov, S. A. Dvoretzky, V. I. Gavrilenko, W. Knap, F. Teppe, and J. Lusakowski, Magnetoconductivity and terahertz response of a hgcdte epitaxial layer, *Sensors* **18**, 4341 (2018).
- [22] D. Soranzio, E. Abreu, S. Houver, J. Dössegger, M. Savoini, F. Teppe, S. Krishtopenko, N. N. Mikhailov, S. A. Dvoretzky, and S. L. Johnson, *Roles of band gap and kane electronic dispersion in the thz-frequency nonlinear optical response in hgcdte* (2024).
- [23] G. Y. Vasileva, Y. B. Vasilyev, A. A. Greshnov, N. N. Mikhailov, A. A. Usikova, C. Belke, and R. J. Haug, Giant magnetoresistance in gapless hgcdte with kane fermions, *EPL (Europhysics Letters)* **128**, 47001 (2020).
- [24] D. B. But, M. Mittendorff, C. Consejo, F. Teppe, N. N. Mikhailov, S. A. Dvoretzky, C. Faugeras, S. Winnerl, M. Helm, W. Knap, M. Potemski, and M. Orlita, Suppressed auger scattering and tunable light emission of landau-quantized massless kane electrons, *Nature Photonics* **13**, 783 (2019).
- [25] S. D. Ganichev and W. Prettl, *Intense Terahertz Excitation of Semiconductors* (Oxford University Press, Oxford, 2005).
- [26] V. V. Bel'kov and S. D. Ganichev, Magneto-gyrotropic effects in semiconductor quantum wells, *Semicond. Sci. Technol.* **23**, 114003 (2008).
- [27] E. L. Ivchenko and S. D. Ganichev, *Spin Physics in Semiconductors*, edited by M. I. Dyakonov (Springer, 2018) 281-328.
- [28] S. D. Ganichev, W. Prettl, and P. G. Huggard, Phonon assisted tunnel ionization of deep impurities in the electric field of far-infrared radiation, *Phys. Rev. Lett.* **71**, 3882 (1993).
- [29] S. D. Ganichev, I. N. Yassievich, W. Prettl, J. Diener, B. K. Meyer, and K. W. Benz, Tunneling ionization of AutolocalizedDX-centers in terahertz fields, *Phys. Rev. Lett.* **75**, 1590 (1995).
- [30] S. D. Ganichev, E. Ziemann, T. Gleim, W. Prettl, I. N. Yassievich, V. I. Perel, I. Wilke, and E. E. Haller, Carrier tunneling in high-frequency electric fields, *Phys. Rev. Lett.* **80**, 2409 (1998).
- [31] S. D. Ganichev, V. V. Bel'kov, S. A. Tarasenko, S. N. Danilov, S. Giglberger, C. Hoffmann, E. L. Ivchenko, D. Weiss, W. Wegscheider, C. Gerl, D. Schuh, J. Stahl, J. D. Boeck, G. Borghs, and W. Prettl, Zero-bias spin separation, *Nat. Phys.* **2**, 609 (2006).
- [32] S. D. Ganichev, Y. V. Terent'ev, and I. D. Yaroshetskii, Photon-drag photodetectors for the far-ir and sub-millimeter regions, *Pis'ma Zh. Tekh. Fiz.* **11**, 46 (1985), [Sov. Tech. Phys. Lett. **11**, 20 (1989)].
- [33] At low temperatures we were forced to reduce power by 10^6 . The observed nonlinearity is of independent interest but is out of scope of the present paper.
- [34] E. L. Ivchenko, Y. B. Lyanda-Geller, and G. E. Pikus, Magneto-photogalvanic effects in noncentrosymmetric crystals, *Ferroelectrics* **83**, 19 (1988).
- [35] V. V. Bel'kov, S. D. Ganichev, E. L. Ivchenko, S. A. Tarasenko, W. Weber, S. Giglberger, M. Olteanu, H. P. Tranitz, S. N. Danilov, P. Schneider, W. Wegscheider, D. Weiss, and W. Prettl, Magneto-gyrotropic photogalvanic effects in semiconductor quantum wells, *J. Phys. Condens. Matter* **17**, 3405 (2005).
- [36] P. Olbrich, C. Zoth, P. Vierling, K.-M. Dantscher, G. V. Budkin, S. A. Tarasenko, V. V. Bel'kov, D. A. Kozlov, Z. D. Kvon, N. N. Mikhailov, S. A. Dvoretzky, and S. D. Ganichev, Giant photocurrents in a dirac fermion system at cyclotron resonance, *Phys. Rev. B* **87**, 235439 (2013).
- [37] C. Zoth, P. Olbrich, P. Vierling, K.-M. Dantscher, V. V. Bel'kov, M. A. Semina, M. M. Glazov, L. E. Golub, D. A. Kozlov, Z. D. Kvon, N. N. Mikhailov, S. A. Dvoretzky, and S. D. Ganichev, Quantum oscillations of photocurrents in HgTe quantum wells with dirac and parabolic dispersions, *Phys. Rev. B* **90**, 205415 (2014).
- [38] E. L. Ivchenko, Y. B. Lyanda-Geller, G. E. Pikus, and R. Y. Rasulov, Magnetoinduced photogalvanic effect in semiconductors, *Sov. Phys. – Semicond.* **18**, 55 (1984).
- [39] E. M. Lifshitz and L. P. Pitaevskii, *Physical Kinetics* (Butterworth-Heinemann, Oxford, 1981).
- [40] S. S. Krishtopenko, I. Yahniuk, D. B. But, V. I. Gavrilenko, W. Knap, and F. Teppe, Pressure- and temperature-driven phase transitions in HgTe quantum wells, *Physical Review B* **94**, 245402 (2016).
- [41] G. Abstreiter, J. P. Kotthaus, J. F. Koch, and G. Dorda, Cyclotron resonance of electrons in surface space-charge layers on silicon, *Phys. Rev. B* **14**, 2480 (1976).
- [42] K. Chiu, T. Lee, and J. Quinn, Infrared magneto-transmittance of a two-dimensional electron gas, *Surf. Sci.* **58**, 182 (1976).
- [43] S. A. Mikhailov, Microwave-induced magnetotransport phenomena in two-dimensional electron systems: Importance of electrodynamic effects, *Phys. Rev. B* **70**, 165311 (2004).
- [44] Q. Zhang, T. Arikawa, E. Kato, J. L. Reno, W. Pan, J. D. Watson, M. J. Manfra, M. A. Zudov, M. Tokman, M. Erukhimova, A. Belyanin, and J. Kono, Superradiant decay of cyclotron resonance of two-dimensional electron gases, *Phys. Rev. Lett.* **113**, 047601 (2014).
- [45] T. Herrmann, I. A. Dmitriev, D. A. Kozlov, M. Schneider, B. Jentzsch, Z. D. Kvon, P. Olbrich, V. V. Bel'kov, A. Bayer, D. Schuh, D. Bougeard, T. Kuczmik, M. Oltcher, D. Weiss, and S. D. Ganichev, Analog of microwave-induced resistance oscillations induced in GaAs heterostructures by terahertz radiation, *Phys. Rev. B* **94**, 081301 (2016).
- [46] A. V. Ikonnikov, M. S. Zholudev, V. I. Gavrilenko, N. N. Mikhailov, and S. A. Dvoretzky, Magnetoabsorption in narrow-gap HgCdTe epitaxial layers in the terahertz range, *Semiconductors* **47**, 1545 (2013).
- [47] C. L. Littler, D. G. Seiler, and M. R. Loloee, Magneto-optical investigation of impurity and defect levels in HgCdTe alloys, *Journal of Vacuum Science and Tech-*

- nology A: Vacuum, Surfaces, and Films **8**, 1133 (1990).
- [48] D. A. Kozlov, Z. D. Kvon, E. B. Olshanetsky, N. N. Mikhailov, S. A. Dvoretzky, and D. Weiss, Transport properties of a 3d topological insulator based on a strained high-mobility HgTe film, *Phys. Rev. Lett.* **112**, 196801 (2014).
- [49] M. Savchenko, D. Kozlov, N. Mikhailov, S. Dvoretzky, and Z. Kvon, Weak antilocalization in partially relaxed 200-nm hgte films, *Physica E: Low-dimensional Systems and Nanostructures* **129**, 114624 (2021).
- [50] C. Fau, J. F. Dame, M. de Carvalho, J. Calas, M. Averous, and B. A. Lombos, Three-band model applied to narrow-gap HgCdTe, *physica status solidi (b)* **125**, 831 (1984).